JAERI 1137

JAERI 1137

Itinerant Antiferromagnetism in Chromium Alloys

July 1967

日本原子力研究所

Japan Atomic Energy Research Institute

日本原子力研究所は，研究成果，調査結果の報告のため，つぎの3種の研究報告書を，それぞれの通しナンバーを付して，不定期に公刊しております．

1. 研究報告	まとまった研究の成果あるいはその一部における重要な結果の報告	JAERI 1001-3999
2. 調査報告	総説，展望，紹介などを含め，研究の成果，調査の結果をまとめたもの	JAERI 4001-5999
3. 資　　料	研究成果の普及，開発状況の紹介，施設共同利用の手引など	JAERI 6001-6999

このうち既刊分については「JAERI レポード一覧」にタイトル・要旨をまとめて掲載し，また新刊レポートは「原研びぶりお」でその都度紹介しています．これらの研究報告書に関する頒布，版権，複写のお問合せは，日本原子力研究所技術情報部（茨城県那珂郡東海村）あてお申し越しください．

Japan Atomic Energy Research Institute publishes the nonperiodical reports with the following classification numbers:

1. **JAERI** 1001-3999 Research reports,
2. **JAERI** 4001-5999 Survey reports and reviews,
3. **JAERI** 6001-6999 Information and Guiding Booklets.

Any inquiries concerning distribution copyright and reprint of the above reports should be derected to the Division of Technical Information, Japan Atomic Energy Research Institute, Tokai-mura, Naka-gun, Ibaraki-ken, Japan.

編集兼発行　日本原子力研究所

Itinerant Antiferromagnetism in Chromium Alloys*

Summary

The electrical resistivity and the powder nentron diffraction patterns for Cr-V, Cr-Mn and Cr-Mo binary alloys as well as Cr-V-Mn ternary alloys have been measured at various temperatures. From these measurements we have deduced the type of magnetic structure and estimated the corresponding physical quantities such as Néel temperature, magnetic moment and wave vector of spin density wave (SDW) state. The results are compared with each other on the same scale of effective concentration, i. e. Mn concentration subtracted by V concentration in units of atomic percent. The overall results, expressed as a unique function of effective concentration, show a good agreement between Cr-V, Cr-Mn binary alloys and Cr-V-Mn ternary alloys. The main conclusion deduced from the experimental results is a positive, though not decisive, support for the validity of rigid band approximation. The results are further discussed in terms of the three kinds of SDW model for chromium; free electron model, single-band model and two-band model. The bearing of the Fermi surface in its relation with Brillouin zone boundaries is analyzed on the basis of extended HUME-ROTHERY'S rule. Following this analysis a possible explanation for incommensurable-to-commensurable transition in Cr-Mn and Cr-V-Mn alloys as a function of electron concentration is proposed.

May, 1967

S. KOMURA
Japan Atomic Energy Research Institute

クロム合金におけるバンド電子の反強磁性

要　旨

二元系合金 Cr-V, Cr-Mn および Cr-Mo と三元系合金 Cr-V-Mn に対していろいろな温度で電気抵抗および粉末中性子回折像を測定した．これらの測定から磁気構造の型を推定し，スピン密度波(SDW)状態の対応する物理量，たとえばネール温度，磁気モーメントおよび波動ベクトルを求めた．その結果を互いに実効濃度――すなわち原子パーセントであらわした Mn 濃度マイナス V 濃度――で比較した．結果はおおよそ実効濃度の単一関数としてあらわされ，Cr-V, Cr-Mn 二元系合金と Cr-V-Mn 三元系合金とは互いによく一致している．この結果は剛性バンド近似の妥当性を支持している．この結果はさらにクロムに対する三種類の SDW 模型，すなわち自由電子模型，1バンド模型および2バンド模型を用いて議論した．フェルミ面とブリュアン域境界との関係の意味を，拡張されたヒューム=ロザリ則にもとづいて解析した．この解析にしたがって Cr-Mn および Cr-V-Mn合金における電子濃度の関数としての SDW―反強磁性間転移を説明する機構を提唱した．

1967年5月

日本原子力研究所　好　村　滋　洋

* This paper is submitted by the author as a thesis to the Faculty of Science, University of Tokyo in partial fulfillment of the requirements for the degree of Doctor of Philosophy, 1967.

Contents

目　　次

1. Introduction

1.1 Historical survey of experimental studies

1.1.1 Chromium metal

The early powder neutron diffraction studies on various transition metals by SHULL and WILKINSON[1] demonstrated that in chromium metal the magnetic moment of 0.40 Bohr magnetons per atom was arranged in a simple antiferromagnetic array. The spin moments at the corner and center atoms in the bcc structure were coupled antiparallel. They found that the Néel temperature was 200°C, in contrast with 37°C and −150°C for the anomalies in various physical properties[2), 3)], such as electrical resistivity, thermal expansion and Young's modulus. BEAUMONT et al[4] measured the specific heat of chromium and found a small entropy change of 0.0044 cal/gm atom deg. at the transition temperature of 38.5°C. This latter fact is believed to be an indication of itinerant character of 3d-electrons in Cr metal. In a number of later neutron diffraction studies[5),6),7),8)] with single crystal of chromium, it has become apparent that the magnetic properties of this metal are much more complicated than the early studies had indicated.

CORLISS, HASTINGS and WEISS[5] showed in their experiments on a single crystal of chromium that there exists magnetic satellite reflections corresponding to a long-range modulation of the antiferromagnetic moment distribution. This modulation was at first interpreted in terms of an anti-phase domain structure. They found a Néel temperature of about 35°C which coincides with other physical anomalies mentioned above. BYKOV et al[6] also found a Néel temperature at 44°C as well as another new transition temperature at −115°C as expected from the measurements of other physical properties. The similar measurements by BACON[7] showed that the Néel temperature is sensitive to differences of domain size and strains brought about by different methods of crystal growth and subsequent treatment. His results gave a Néel temperature of 40°C for strain-free single crystal of pure chromium in agreement with the transition temperature of other physical properties. He also found that the period of the modulation is 22 unit cells well below the Néel temperature. SHIRANE and TAKEI[8] tried to observe the third order satellites, which is characteristic of the anti-phase domain structure. But he observed no such higher order satellites and suggested a model in which the magnetic moments are perpendicular to the wave vector of the sinusoidal modulation of the spin density wave (SDW) below the Néel temperature of 310°K down to the "spin flip" temperature of 121°K. They proposed that below 121°K the magnetic moments change their orientation and lie parallel to the wave vector.

The absence of paramagnetic scattering from powdered isotope Cr^{52} above the Néel temperature by WILKINSON et al[9] indicated that the localized atomic magnetic moments do not exist in metallic chromium above the Néel temperature. This fact is thought to be a strong evidence for the itinerant character of the magnetic moment of chromium in contrast with the localized one.

ARROTT et al[10] found the first-order magnetic phase change at the Néel temperature of 312°K in chromium. In their chromium specimen cooled through the Néel temperature under a magnetic field, they found a tetragonal "single-Q" state in which a single domain with a definite wave vector Q for the SDW is defined in contrast with usual cubic "triple-Q" state in non-field-cooled specimen. BASTOW and STREET[11] confirmed the results that field cooling favors the growth of domains with its SDW vector parallel to the direction of the field. They also

found that in stress cooling the development of domains with its SDW vector parallel to the direction of compressive stress is inhibited.

1.1.2 Chromium alloys

On the other hand, the electrical resistivity measurements on chromium alloys with 1 atomic percent addition of V, Mn, Fe, Co or Ni by DE VRIES[12] showed appreciable changes in the Néel temperature, indicating that the magnetic properties of chromium is highly sensitive to the addition of other 3d transition metals. In Cr-V alloys 1 percent addition of V reduces T_N to 225°K, while in Cr-Mn alloys 1 percent of Mn increases T_N to 465°K.

In subsequent studies on the electrical resistivity by TAYLOR[13] and nuclear magnetic resonance by DRAIN[14] in Cr-V alloys, it was found that the Néel temperature of chromium metal decreases rapidly with increasing vanadium concentration. The extrapolation of the Néel temperature-vanadium concentration curves to absolute zero temperature reads 4 atomic percent of vanadium. The electrical resistivity and neutron diffraction studies on Cr-Mn alloys by KASPER and WATERSTRAT[15] and later by HAMAGUCHI and KUNITOMI[16] indicated that the Néel temperature of Cr-Mn alloy increases up to 667°K at 7 atomic percent addition of manganese and reaches 768°K at 25. 3 atomic percent of manganese. The Néel temperature remains almost constant for Cr-Mn alloys with more than 25 atomic percent Mn and is 793°K for 48 atomic percent Mn. The data for the electrical resistivity of Cr-V alloys were later supplemented by BJERRUM MØLLER et al[17]. The experimental data of NMR on Cr-V alloys by BARNES and GRAHAM[18] also determined the Néel temperature accurately for this alloy system.

The electrical resistivity of Cr-Mo alloys were measured by HEINIGER et al[19] and by SUZUKI[20]. According to their results the Néel temperature of Cr-Mo alloys decreases gradually with addition of molybdenum at a rate of −12°K/atomic percent in contrast with either the rapid decrease of the Néel temperature in Cr-V or rapid increase in Cr-Mn alloys. The extrapolation of Néel temperature-Molybdenum concentration curve to absolute zero temperature amounts 25 atomic percent of molybdenum.

We have undertaken in a series of papers the neutron diffraction studies on powdered Cr-V[21], C-Mn[22] and Cr-Mo[23] binary alloys together with Cr-V-Mn[24] ternary alloys. These papers constitute the basis for the present thesis. These results are further confirmed by other authors[17),25),26] through independent diffraction studies on the single crystal of chromium alloys. Their results are essentially in good agreement with our results.

1.2 Divergent opinions on the properties of chromium

1.2.1 Three models for chromium

Several theories have been proposed to explain the unusual magnetic properties of chromium. OVERHAUSER[27] proposed a spin density wave (SDW) model based on the calculation of ground state of free electron gas within HARTREE-FOCK approximation. However he assumed a bare coulomb interaction thus neglecting the correlation effect among the electrons. In line with YOSIDA's suggestion[28] that the Umklapp process of band electrons plays an essential role in stabilizing the helical spin arrangement, TACHIKI and NAGAMIYA[29] calculated the condition for the occurrence of the helical spin arrangement in chromium on the basis of tight binding approximation. Once adjusting the number of electrons to be 0. 5 in the band responsible for the spin arrangement so as to give the magnetic period consistent with that of chromium, they

could predict the variation of the magnetic period with the number of electrons. Besides the above two models for chromium, another model based on the interaction between two different bands was proposed earlier by LOMER[30] and was recently elaborated by FEDDERS and MARTIN[31]. They have shown that if the correlation effect is taken into account the SDW state is not the ground state of free electron gas and that the two-band model would be more plausible to realize the SDW state than the single-band model. Among these three models, namely, a) free electron model by OVERHAUSER, b) single-band model by TACHIKI and NAGAMIYA and c) two-band model by LOMER, it is still a question which model is a correct one.

1.2.2 Rigid band approximation

The three models mentioned in the previous section are based on the collective electron theory of metals. The most important features of these calculations are the relation of the Fermi surface to the Brillouin zone boundaries of the band electrons. The magnetic properties are expected to be modified by changes in the Fermi surface in chromium alloys. Such an analysis naturally requires the rigid band postulate in the alloy systems.

The results of the electronic specific heat measurements on the bcc alloys of Cr-V, Cr-Mn and Cr-Fe by CHENG et al[32] can be interpreted to a surprising extent in terms of a more or less rigid d-band. The degree of filling up of the band with electrons is determined essentially by the average electron concentration of the alloys. From the measured γ vs. electron concentration curve, they could derive the density of d states vs. Fermi energy curve.

MATTHEISS[33] has calculated energy bands for elements of iron transition series in three different crystal structures using augmented plane wave method : fcc (Ar, Co, Ni, Cu), bcc(V, Cr, Fe) and hcp (Ti, Zn). The results exhibit a reasonably smooth variation from element to element, especially for those substances having the same crystal structure. This provides some justification of the rigid band approximation for transition metal and their alloys.

A calculation by LOUCKS[34] on the Fermi surfaces of Cr, Mo and W by the augmented plane wave method has shown that the Fermi surfaces of Cr, Mo and W are almost identical to each other, while there is some difference between Cr and the other two in the detailed shapes. An independent calculation on the Fermi surface of W performed at the same time by MATTHEISS[35] using the same method has indicated the overall agreement with the Loucks' results. Therefore, these results on the calculation of band structure are thought to be most promising at present for understanding the electronic structure in chromium alloys with bcc structure.

All the studies stated above lend some support to the rigid band approximation for the transition series elements. However there are some oppositions against this approximation in the following aspects. There is a specific heat anomaly[32] in some of V-Fe, Cr-Fe and Cr-Mn alloys exhibited in the negative temperature coefficients of the specific heat. There is also an absence[32] of completely quantitative coincidence between the corresponding part of the γ vs. electron concentration curves for the V-Fe, Cr-Fe and Cr-Mn system. These facts require further studies for justification of the rigid band approximation.

1.3 Statement of problems

1.3.1 Problems to be solved

As has been stated in detail in 1. 1 and 1. 2, a number of unusual properties of chromium and its alloys with other transition metals has been discovered experimentally. These phenomena

have been the subject of many theoretical investigations. The three models for chromium have been proposed. Furthermore we have no exact knowledge on the extent to which the rigid band approximation is applicable. This approximation is of considerable value in understanding the properties of chromium in terms of the three models. Such an analysis is expected to enable us to get a basic understanding of the itinerant antiferromagnetism in transition metals and alloys. We therefore set the problems as follows :

1) To what extent is the rigid band approximation in chromium alloys valid ?
2) What kind of models for chromium is applicable to explain the unusual properties of chromium and its alloys ?
3) How the concepts of itinerant antiferromagnetism can be applied in understanding the magnetic properties of transition metals and their alloys ?

In order to solve these problems, we have undertaken to study the magnetic behaviors in Cr–V, Cr–Mn and Cr–Mo binary alloys as well as Cr–V–Mn ternary alloys.

From the foregoing discussions, we can expect the behaviors of Cr–V, Cr–Mn and Cr–Mo binary alloys as follows. On the assumption of rigid band approximation, energy bands and Brillouin zone boundaries in chromium will be little changed by alloying, while the Fermi energy will decrease with addition of V or increase with addition of Mn. Accordingly, several magnetic properties of Cr will be changed as a unique function of average number of 3d electrons. Contrary to Cr–V or Cr–Mn case, the Fermi energy in Cr will remain fixed with addition of Mo, resulting in the magnetic properties unchanged in Cr–Mo alloys.

The above mentioned behaviors of Cr–V, Cr–Mn and Cr–Mo alloys presuppose the rigid band approximation. However the behaviors do not give any positive support for the validity of this approximation.

We have undertaken to study Cr–V–Mn ternary alloys to test the validity of the rigid band approximation. If the rigid band approximation is strictly valid in this alloy system, the magnetic properties of the ternary alloys are determined by the effective concentration defined as the manganese concentration subtracted by the vanadium concentration in units of atomic percent. The ternary alloys with the negative effective concentration should exhibit the behavior identical with that of corresponding Cr–V binary alloys and those with positive effective concentration the behavior identical with that of corresponding Cr–Mn alloys. Any deviation of the behavior of the ternary alloys from that of corresponding binary alloys should be ascribed to the violation of the rigid band approximation in these alloy systems.

In the present study we have measured the temperature dependence of the electrical resistivity and the powder diffraction patterns at various temperature on these binary and ternary alloys, from which we can deduce several magnetic properties of the alloys. These results are compared with each other and especially with those for pure chromium metal. The further implications of the experimental details are discussed in comparison with the three kinds of SDW models for chromium mentioned above together with the validity of rigid band approximation in these alloys.

1.3.2 Plan of the present thesis

Following this introduction of **Chapter 1**, we shall survey in **Chapter 2** the principles of the experiments dealing with the special features of temperature dependence of electrical resistivities and the magnetic scattering intensities of neutrons from oscillatory magnetic structures. We describe in **Chapter 3** the experimental equipments for both electrical resistivity and neutron diffraction measurements together with the sample preparation. In **Chapter 4** the experimental

results of electrical resistivity and neutron diffraction measurements on Cr–V, Cr–Mn, Cr–Mo binary alloys and Cr–V–Mn ternary alloys are described separately. The discussions of the experimental results in connection with the rigid band approximation are given in **Chapter 5**. A comparison of the data with three models for chromium is also made in the same chapter. In the final **Chapter 6**, concluding remarks on the itinerant antiferromagnetism in chromium and its alloys are given. Some comments are also made concerning the prospects for future studies.

2. Principles of Experiment

2.1 Temperature dependence of electrical resistivities

The formulas for electrical resistivities in metals with oscillatory spin structure are given in **Appendix A**. The electrical resistivities of metals with oscillatory structures have a characteristic temperature dependence with its minimum at the Néel temperature. The subsequent increase in resistivity below the Néel temperature is a consequence of the formation of new energy gaps due to the oscillatory structure. The gaps truncate the Fermi surface, thus reducing the number of carriers, i.e. electrons participating in the transport phenomena. A similar mechanism can also be applied to purely antiferromagnetic metals resulting in a similar characteristic temperature dependence of electrical resistivity as explained in **Appendix A**. These circumstances make it possible to determine the Néel temperature in metals with antiferromagnetic or oscillatory structures. The magnitude of increase in the resistivity below the Néel temperature is also useful information on the mangnetic structure under investigation.

2.2 Scattering of neutrons from oscillatory magnetic structures

Several formulas for nuclear and magnetic scattering intensity are given in **Appendix B**. We metion here only the characteristic features of the magnetic scattering from oscillatory magnetic structures.

In the case of oscillatory magnetic structures, the fundamental magnetic peaks disappear and at the same time there appear new satellite reflections in pairs around the disappeared magnetic peaks. Therefore in the case of bcc structure, for example, the antiferromagnetic peaks such as (100) disappear and at the same time there appear new satellite reflections in pairs such as $(1\pm\delta, 0, 0)$, $(1, \pm\delta, 0)$, $(1, 0, \pm\delta)$.

The precision measurements of these satellite reflections enable us to determine the type of oscillatory magnetic structures as illustrated in **Fig. 1** for bcc metals. The transverse sinusoidal structure, for example, is further represented in three dimensional array in **Fig. 2**. Since the pos-

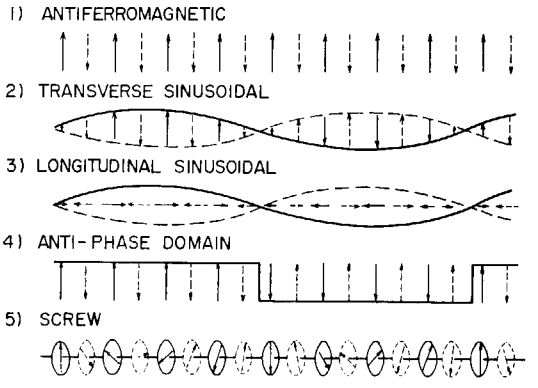

Fig. 1 Various types of spin structures for bcc antiferromagnetic substances. Undotted arrows correspond to corner atoms, while dotted arrows to body-center atoms.

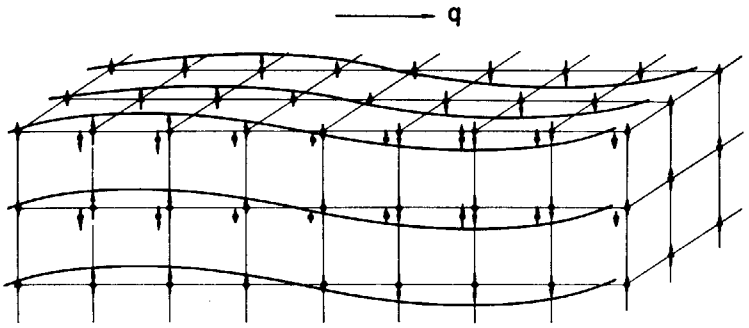

Fig. 2 Three dimensional array of transverse sinusoidal structure in "single-Q" state in Cr

sibility of anti-phase domain structure and screw structure is already rejected in pure Cr, we have only to consider the three types in chromium alloys: a) pure antiferromagnetic, b) transverse sinusoidal and c) longitudinal sinusoidal structure. As has been described in detail in **Appendix B**, a θ-2θ drive measurement on powdered sample using unpolarized neutrons will give rise to a single peak at (100) in both pure antiferromagnetic and longitudinal sinusoidal structure, whereas the same measurement will give rise to three peaks in the ratio 1 : 2 : 1 in transverse sinusoidal structure. If the maximum moment in sinusoidal structure, including both transverse and longitudinal, put equal to the moment in antiferromagnetic structure, the total intensity of the sinusoidal structure is half that of antiferromagnetic structure.

Careful measurements of the satellite reflections followed by an appropriate analysis of the data can establish the values for the average magnetic moment and the wave vector of the pertinent type of magnetic structures.

3. Experimental Procedures[36]

3.1 Electrical resistivity measurements

The temperature dependence of the electrical resistivity was measured by means of the conventional 4-terminals method using high precision potentiometer. The temperature of the specimens was varied from liquid nitrogen temperature up to 500°C covering always the Néel temperature in increasing temperature as determined by Cu-constantan thermo-couple. Due to the irregularites of the size of the specimens, the absolute values for the electrical resistivity may involve some errors, while the relative values at different temperatures on the same specimen are considered to be highly reliable. These circumstances permit the accurate determination of Néel temperature from the temperature dependence of the electrical resistivity.

3.2 Neutron diffractometer

The horizontal and vertical views of the neutron diffractometer[37] are given in **Fig. 3** and **4**, respectively. The diffractometer has been installed at JRR-2 in JAERI, which is operated at 10 MW. The monochromator used was a lead single crystal with (111) reflecting plane. The neutron wave-length used throughout the experiment was 0.98 A. This relatively low value of wave-length was chosen in order to avoid the second order contamination of (200) nuclear reflection in precision measurement of the intensity of (100) magnetic reflection. This

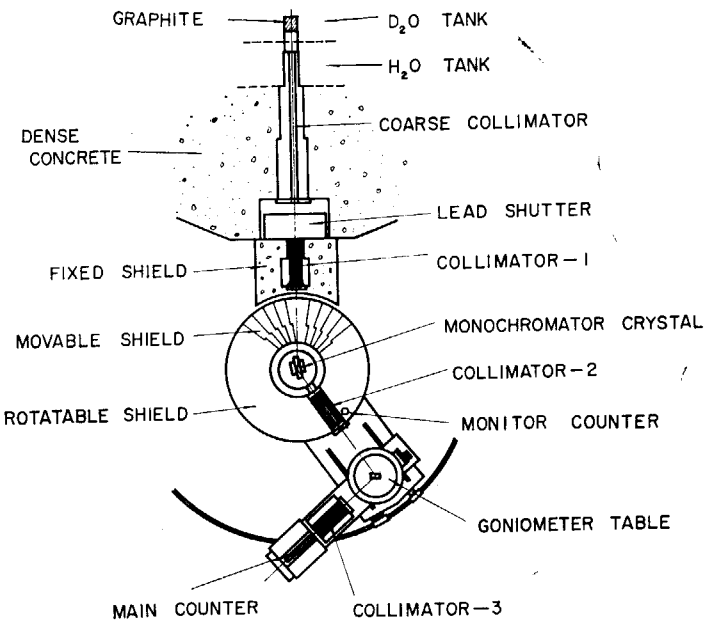

Fig. 3 Horizontal view of the neutron diffractometer in JAERI

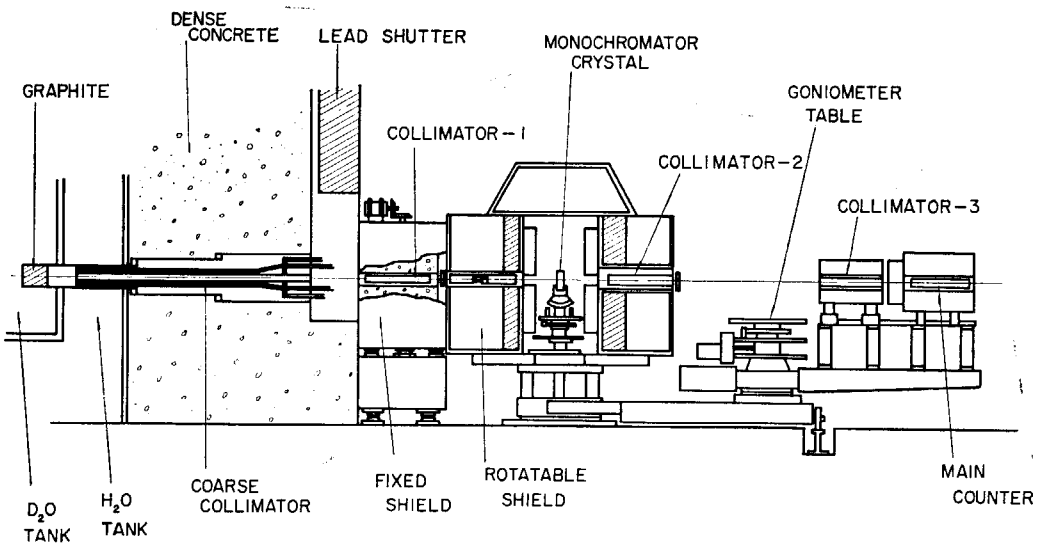

Fig. 4 Vertical view of the neutron diffractometer in JAERI

choice of the wave length made the second order contamination practically negligible. The cross section of the neutron beam was a square of 4cm×4cm. The angular resolution of first and third collimtors was chosen to be 30 minutes, while the second collimator was removed.

3.3 Cryostat for neutron diffraction

The temperature of the sample is controlled in the cryostat as shown in **Fig. 5**. The sample is suspended below a liquid helium reservoir which provides a continuous variation of temperature from liquid helium temperature up to 120°C. The temperature is measured by Cu-constantan thermo-couple as in the electrical resistivity measurements. About 40 grams of the powdered sample were put in the sample holder of 1.8cm diameter with 5cm height made of thin aluminum.

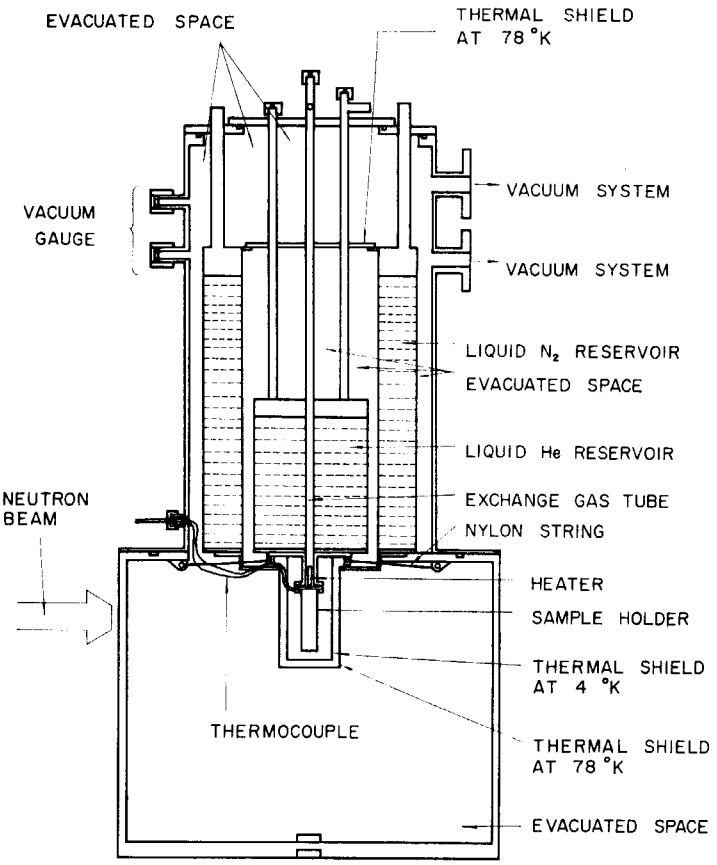

Fig. 5 Vertical view of the cryostat for neutron diffraction

3.4 Neutron diffraction measurements

For each specimen the powder neutron diffraction patterns for wide range of scattering angle were measured including the (110) nuclear reflection, which was taken as the standard of the scattering intensities of the specimen. The diffraction patterns of (100) magnetic reflection were measured in precision at various temperatures from liquid helium temperature up to 400° K. However in most cases the measurements were made at liquid nitrogen temperature.

Unfortunately the scattering angle of (200) reflection of aluminum of the specimen holder coincides with that of (110) nuclear reflection of the specimens. It was therefore necessary to correct for this overlap in determining the scattering intensities of (110). For this purpose we measured the linear absorption coefficient of neutrons through each speimen by means of a narrow neutron beams of about 1 mm in width.

Comparing the intensities of coherent magnetic scattering near the position of (100) reflection with those of coherent nuclear reflection of (110), we can calculate the magnetic scattering cross section. In this calculation, the nuclear scattering amplitude for Cr is taken to be 0.352 $\times 10^{-12}$cm[38]. The magnetic form factor of Cr is assumed to be the same as the experimental values for Mn^{2+} [39]. This assumption is further justified by the recent measurements[40] on the magnetic form factor in Cr-Mn alloys with 1.7 atomic percent Mn. We thus obtained the values for average magnetic moment μ per atom in either antiferromagnetic or sinusoidal spin structures.

From the angular separations between the central and side peaks in those diffraction patterns having three peaks, we can calculate the wave vector q for sinusoidal spin modulation.

3.5 Sample preparation

Pure chromium (99.999%), pure vanadium (99.8%) pure molybdenum (99.9%) and electrolytic manganese (99.9%) of proper composition were melted in an arc furnace under argon atmosphere. About twice the amount of electrolytic manganese was necessary to get the desired compositon, because the half of added manganese vanished away from the ingots during the melting process on account of the high vapour pressure of liquid manganese.

The specimens for the electrical resistivity measurements were cut from the ingots into proper dimensions : about 1.5 mm × 2.5 mm × 20 mm. The rest of the ingots was crushed into coarse powder of less than 1 mm diameter in a steel mill and then in an agate mortar for neutron diffraction specimens. The contamination of the specimen from the pieces of steel caused during the crushing process was eliminated by sweeping the specimen with a permanent magnet. The specimens for neutron diffraction studies together with those for electrical resistivity measurements of the same ingots were put into an evacuated quartz tube and homogenized at 1050° C for 1 week.

The ultimate values for concentrations of vanadium, manganese, and molybdenum determined by a series of chemical analysis[41] are given in TABLE 1. The effective concentration defined as

TABLE 1 The second column gives the concentration of vanadium, manganese, molybdenum and effective concentration (atomic percent) of each specimen as determined from the chemical analysis. The third column gives types of magnetic structures (AF_0=Antiferromagnetic structure, AF_1=Transverse sinusoidal structure, AF_2=Longitudinal sinusoidal structure, AF_0+AF_1=Coexistence of both AF_0 and AF_1 structures). For lower temperature the type of structure is given at the left side of the column, while for higher temperature it is given at the right side of the column. The last column gives the physical quantities such as Néel temperature T_N (degrees Kelvin), average magnetic moment μ (Bohr magnetons) and wave vector q (in units of $2\pi/a$) of the SDW state for each specimen with estimated errors.

		Concentration				Magnetic structure		Physical quantities		
		V	Mn	Mo	Effective	Low temp.	High temp.	T_N	μ	q
Pure	Cr	0	0	0	0	AF_2	AF_1	310	0.40±0.02	0.9518
Cr-V	(1)	0.45	0	0	−0.45	AF_1		268±5	0.36±0.03	0.9431±0.0025
	(2)	1.00	0	0	−1.00	AF_1		220±5	0.28±0.03	0.9300±0.0025
Cr-Mn	(1)	0	0.50	0	+0.50	AF_2, AF_1, AF_0+AF_1, AF_0		390±10	0.47±0.02	0.9700±0.0025
	(2)	0	0.70	0	+0.70			440±5		
	(3)	0	0.74	0	+0.74	AF_0+AF_1	AF_0	422±5	0.54±0.02	0.9700±0.0025
	(4)	0	1.85	0	+1.85			545±5		
	(5)	0	2.1	0	+2.1	AF_0		520±5	0.67±0.02	1.0000
Cr-Mo	(1)	0	0	3.0		AF_1		278±5	0.35±0.02	0.9475±0.0025
	(2)	0	0	5.6		AF_1		250±5		0.9450±0.0025
	(3)	0	0	7.6		AF_1		215±5	0.27±0.02	0.9425±0.0025
Cr-V-Mn	(1)	0.40	0.34	0	−0.06	AF_1		290±5	0.38±0.02	0.9450±0.0025
	(2)	0.54	0.86	0	+0.32	AF_1		360±10	0.39±0.02	0.9550±0.0025
	(3)	0.51	1.07	0	+0.56	AF_1		410±10	0.44±0.02	0.9575±0.0025
	(4)	0.59	1.18	0	+0.59	AF_0		430±10	0.65±0.02	1.0000
	(5)	0.54	1.66	0	+1.12	AF_0		470±5	0.69±0.02	1.0000
	(6)	0.57	2.47	0	+1.90	AF_0		526±5	0.67±0.02	1.0000
	(7)	0.52	3.60	7	+3.08	AF_0		600±5		

the manganese concentration subtracted by the vanadium concentration in units of atomic percent are also given for Cr–V, Cr–Mn and Cr–V–Mn alloy systems.

Two specimens for Cr–V with 0. 45 and 1. 00% V, five specimens for Cr–Mn from 0. 50 up to 2. 1% Mn and three specimens for Cr–Mo from 3. 0 up to 7. 6% Mo were prepared. Fixing the V concentration to about 0. 5%, seven specimens of Cr–V–Mn with the various Mn concentration from 0. 34 up to 3. 60% were also prepared. The distribution of chemical composition of the prepared specimens for Cr–V, Cr–Mn and Cr–V–Mn alloy systems is expressed in a ternary phase diagram in **Fig. 6.**

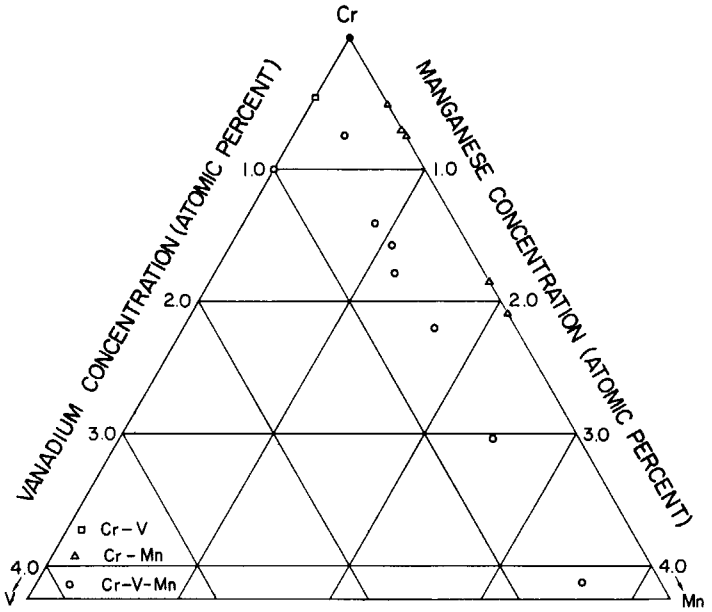

Fig. 6 Distribution of chemical composition of the prepared specimens for Cr–V, Cr–Mn and Cr–V–Mn alloy syetems expressed in a ternary phase diagram

4. Experimental Results

4.1 Electrical resistivity

The temperature dependence of the electrical resistivity for some specimens of Cr–V and Cr–Mn alloys are plotted in **Fig. 7** together with the data for pure Cr[13]. The electrical resistivity data for the seven Cr–V–Mn ternary alloys are shown in **Fig. 8.** The Néel tempertures for each specimen were deduced from these curves. If there is a well defined minimum in the resistivity–temperature curve, the determination of the Néel temperature is unique as in the specimens of Cr–V–Mn (1), (5), (6) and (7). However if there is not a well defined minimum in the curve as in the specimens of Cr–V–Mn (2), (3) and (4), the Néel temperature was determined as such at which deviation from the linear dependence observed at higher temperature becomes to be appreciably large. In this case the estimated errors are larger than the former.

The values for the Néel temperature for each specimen thus determined are listed in **Table 1** together with estimated errors. The same are plotted in **Fig. 9** as a function of effective concentration as well as the data already obtained by various other authors on Cr–V and Cr–Mn binary alloys[12),13),18)] for comparison. It is surprising that these points seem to lie on a

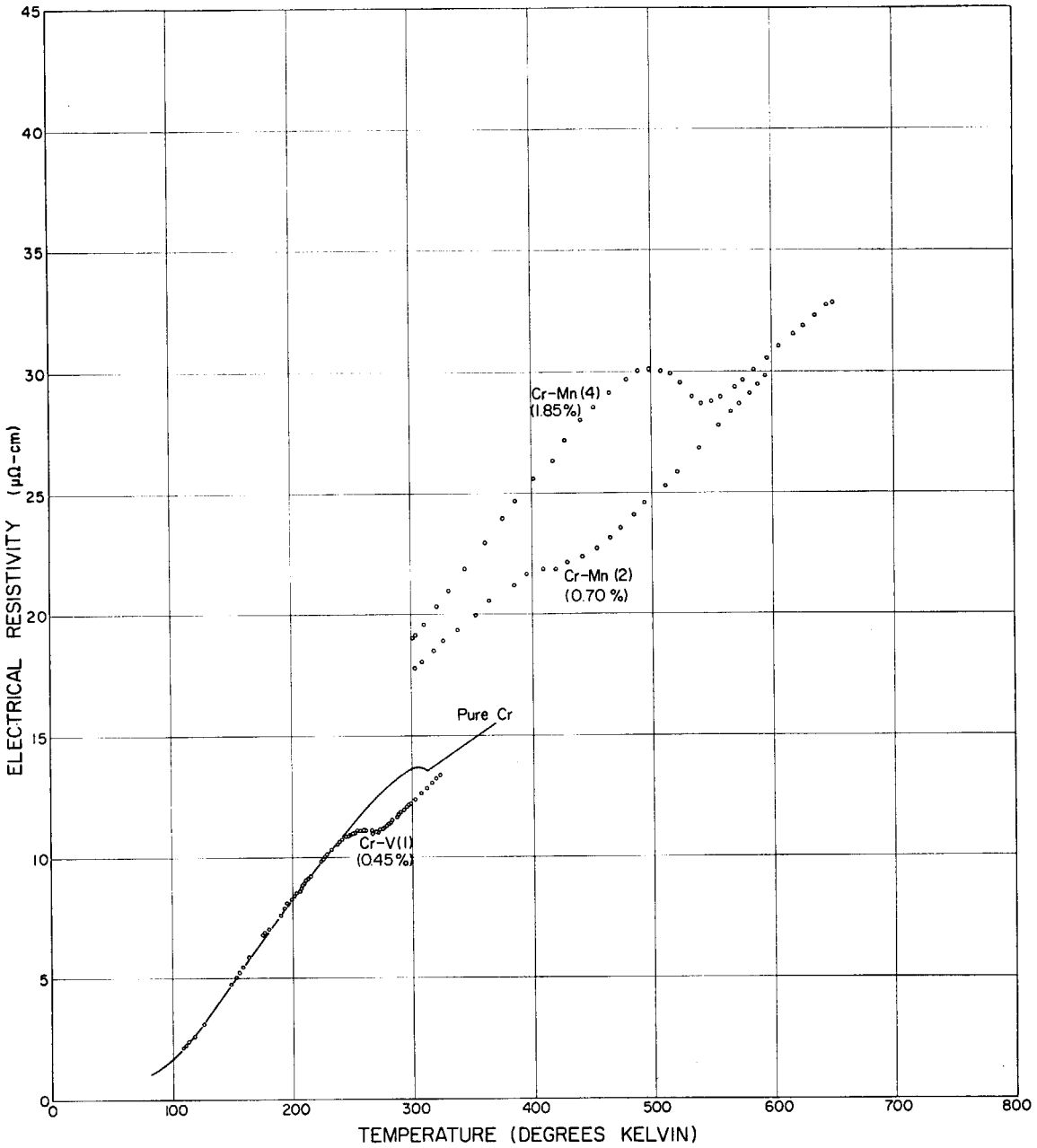

Fig. 7 Temperature dependence of electrical resistivity for Cr–V and Cr–Mn alloys together with that for pure Cr for comparison

single smooth curve on the whole. It is noticed that there is a kink of the curve at the effective concentration of 0.6%.

Comparing **Fig. 7** and **8** with each other, we should notice that the magnitude of resistivity in Cr–V–Mn ternary alloys is slightly larger than that in corresponding Cr–V or Cr–Mn binary alloys. This fact indicates that in the ternary alloys the impurity resistance ρ_i is larger than the binary alloys due to the presence of the same amount of V and Mn to be cancelled by each other.

The electrical resistivity for Cr–Mo alloy system was not measured. The Néel temperatures for these alloys were determined from the data by SUZUKI[20] who has given the Néel temperature as a function of molybdenum concentration at a rate of $-12°$K/atomic percent. The values for Néel temperature thus determined are also included in TABLE 1.

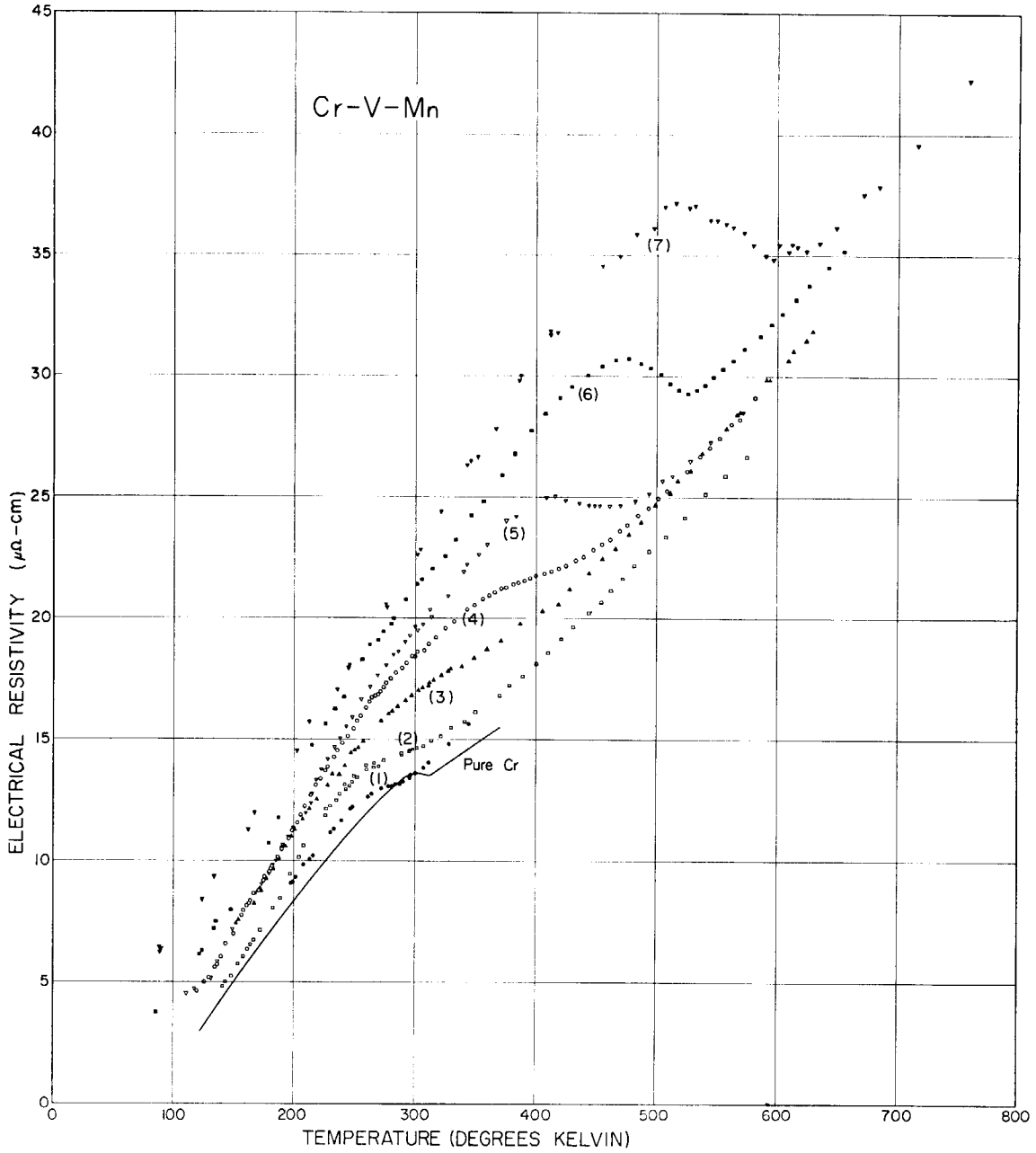

Fig. 8 Temperature dependence of electrical resistivity for Cr–V–Mn alloys together with that for pure Cr for comparison

4.2 Neutron diffraction

4.2.1 Cr-V alloys (KOMURA and KUNITOMI, 1965)[21),22)]

Powder diffraction patterns of (100) satellites for Cr–V (1) at various temperatures are shown in **Fig. 10**. In the pattern obtained at 78° K, three peaks are observed indicating a transverse sinusoidal structure. The pattern obtained at 250° K, which is very close to Néel temperature, has no evidence of diffraction peaks. The pattern taken at intermediate temperature of 197° K shows three peaks vaguely. The temperature dependence of the intensities fit well with the Brillouin function with $S=1/2$. The integrated intensities are slightly smaller than those in Cr. The angular separation between the central and side peaks for Cr–V (1) is slightly larger than that for Cr and increases with decreasing temperature as in Cr. No spin-flip from

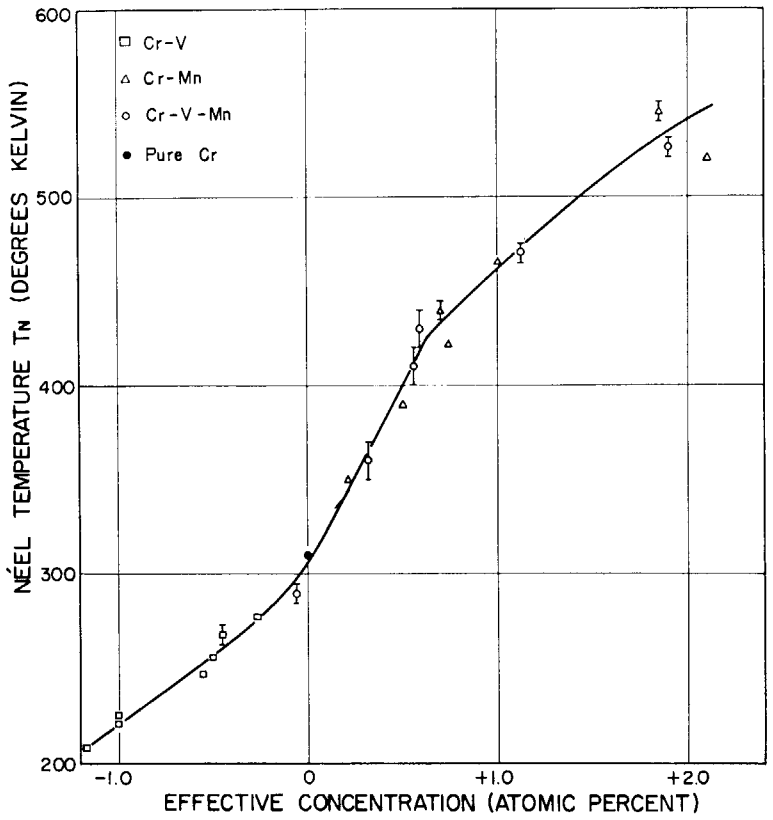

Fig. 9 Concentration dependence of Néel temperature T_N for pure Cr, Cr-V, Cr-Mn and Cr-V-Mn alloys

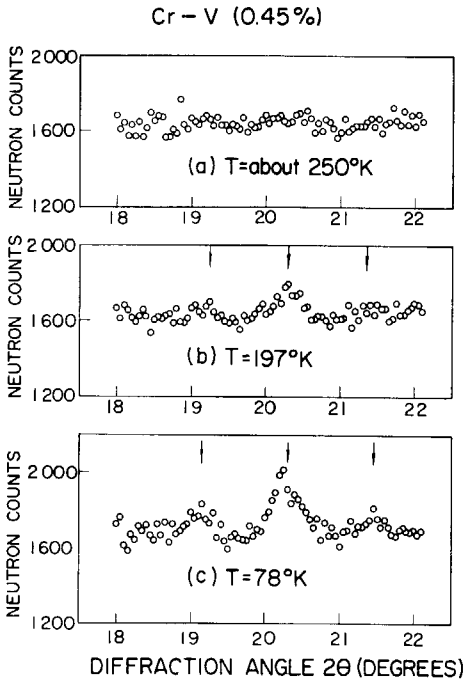

Fig. 10 Powder diffraction patterns of (100) satellites for Cr-V (1) at various temperatures

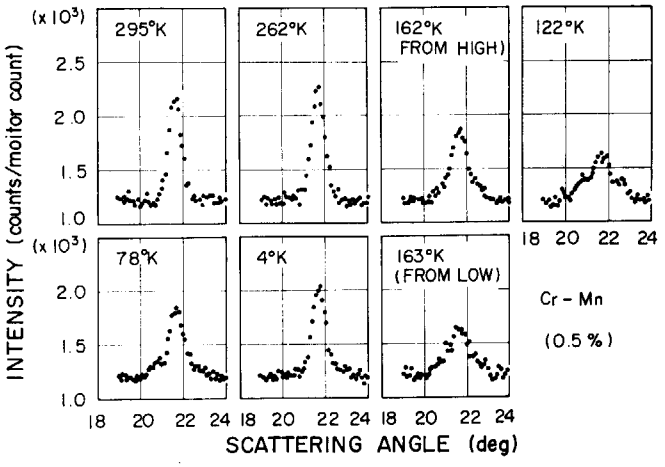

Fig. 11 Diffraction patterns of Cr-Mn (1). "From Low" ("From High") means that the sample is warmed up (cooled down) from the low (high) temperature to the measuring temperature.

transverse to longitudinal sinusoidal structure could be observed down to 78° K, at which temperature Cr completely finishes the spin-flip.

For Cr-V (2) the diffraction patterns are quite similar to Cr-V (1) except that the intensities are slightly more weak and the angular separations are slightly larger.

4.2.2 Cr-Mn alloys (HAMAGUCHI, KOEHLER and WOLLAN, 1965)[22]

The behavior of diffraction patterns for Cr-Mn (1) at various temperatures is quite unusual. These patterns are shown in **Fig. 11**. At or above room temperature it shows a single peak corresponding to a simple antiferromagnetic structure (hereafter abbreviated as AF_0). At temperatures lower than 250° K, however, the peak height of the (100) reflection begins to decrease and two side peaks begin to appear. The intensity of the side peaks reaches a maximum at about 140° K, which corresponds to the minimum intensity of the central (100) peak. The diffraction pattern at this temperature can be interpreted in term of transverse sinusoidal structure (hereafter abbreviated as AF_1). As is clearly shown in **Fig. 12** below 250° K, not only the intensity of the central peak but also the total integrated intensity including the central and the two side peaks begins to decrease and has a minimum at 140° K. Below 100° K the intensity of the central peak increases and that of the two side peaks decreases until 50° K where the side peaks entirely disappear. At liquid helium temperature there is only a single peak, the peak height and the integrated intensity of which are smaller than those at room temperature.

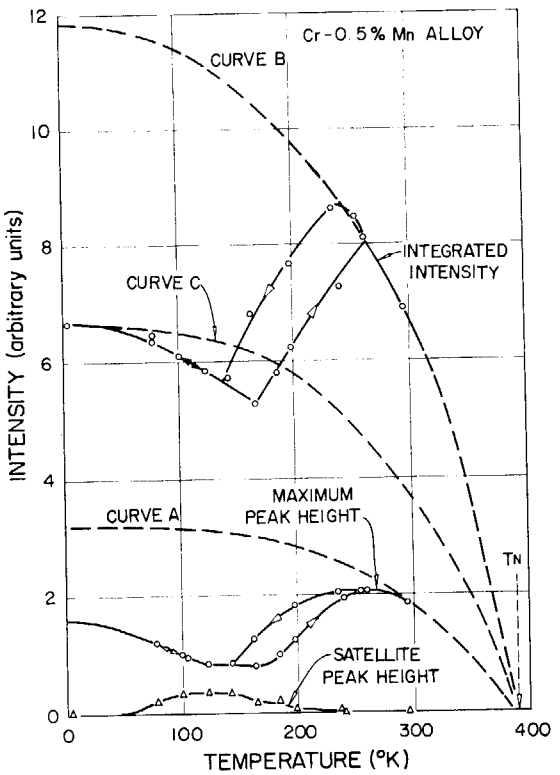

Fig. 12 Temperature dependence of intensities of Cr-Mn (1). Curves A, B and C are the extrapolation curves from the room temperature values according to a Brillouin function with $S=1/2$.

The extrapolated values of the integrated intensity at liquid helium temperature from the room temperature value according to the Brillouin function with $S=1/2$ is about twice the measured value at liquid helium temperature. The average magnetic moment obtained from the integrated intensity at liquid helium temperature is 0.46 μ_B which is slightly larger than in Cr. If we assume that the lowest magnetic phase has a longitudinal sinusoidal structure (hereafter abbreviated as AF_2), the maximum amplitude of the spin density wave is $\sqrt{2}\times 0.47=0.67\ \mu_B$ which is in good agreement with the value of 0.68 μ_B obtained by the extrapolation from the room temperature.

There is a temperature hysteresis between the high temperature AF_0 phase and low temperature AF_1 phase as seen in **Fig. 12**. This suggests the coexistence of AF_0 and AF_1 phase (hereafter abbreviated as AF_0+AF_1) and there exists a first order transition between them. From these observations it has been concluded that in Cr-Mn (1) there are four magnetic phases in decreasing temperature : AF_0, AF_0+AF_1, AF_1 and AF_2. In AF_1 phase the estimated value for q is 0.97 in units of $2\pi/a$, which is slightly larger than that in Cr.

In Cr-Mn (3) the situation is less simple than in the previous Cr-Mn (1). There are two magnetic phases : the high temperature AF_0 phase and low temperature AF_0+AF_1 phase. A temperature hysteresis is observed between these two phases. The associated magnetic moment at room temperature in AF_0 phase is 0.45 μ_B which, on extrapolation to absolute zero temperature, becomes 0.54 μ_B. This value may be compared with the observed value of 0.46 μ_B at liquid

helium temperature in $AF_0 + AF_1$ phase. The difference between the extrapolated and measured values at liquid helium temperature may be explained by assuming an appropriate ratio of coexistence of both AF_0 and AF_1 phases.

In Cr–Mn (5) only a central (100) peak and no side peaks are observed at all temperature below the Néel temperature down to liquid helium temperature. The integrated intensity of the central peak follows closely the Brillouin function with $S=1/2$. The associated structure is simply AF_0 phase with a magnetic moment of 0.67 μ_B at liquid helium temperature.

The alloys containing higher concentration of Mn in Cr, for example 7%, 19.3%, 25.3%[16] and 48.0% Mn alloys[15], exhibit only a single peak at (100) position and no side peaks around it. Thus it appears that the magnetic structure of Cr–Mn alloys with 2.1 up to 50% Mn is simply of AF_0 type without oscillatory modulation. With increasing Mn concentration, the associated magnetic moment in this concentration range increases gradually from 0.59 μ_B up to 0.85 μ_B in about the same proportion with the Néel temperature, as it increases from 520°K up to 793°K.

4.2.3 Cr-Mo alloys (KOMURA, KUNITOMI and HAMAGUCHI, 1967)[23]

Typical diffraction patterns for some of the Cr–Mo alloys at liquid nitrogen temerature are given in **Fig. 13** for example. In the patterns three peaks are evidenced. Such type of diffraction patterns were observed for all the specimens examined through the temperature range below the respective Néel temperature down to the liquid nitrogen temperature of 78°K. This type of diffraction patterns corresponds to AF_1 structure.

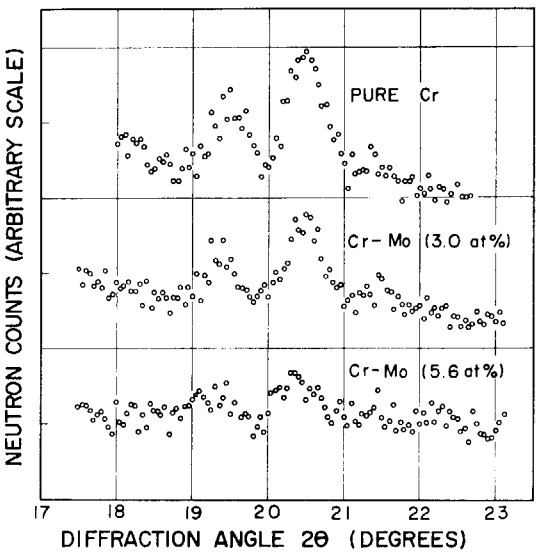

Fig. 13 Diffraction patterns of Cr–Mo (1) and (2) at liquid nitrogen temperature

The average magnetic moment μ and the wave vector q for each specimen was calculated. These values are listed in TABLE 1, together with the estimated errors and plotted in **Fig. 14** as a function of Mo concentration including the data for pure Cr for comparison. As seen in **Fig. 14** μ decreases gradually with addition of Mo in exact proportion to T_N. However the rate of decrease of q is smaller than that of T_N and μ. Thus we can say that the q in Cr–Mo alloys remain almost constant. This is a characteristic feature of Cr–Mo alloys as distinguished from Cr–V or Cr–Mn alloys.

4.2.4 Cr-V-Mn alloys (KOMURA, HAMAGUCHI and KUNITOMI, 1967)[24]

Typical examples of the diffraction patterns for the specimens of Cr–V–Mn (3) and (4) obtained at liquid nitrogen temperature are shown in **Fig. 15**. In the pattern for Cr–V–Mn (3) three peaks are observed, which corresponds to AF_1 structure. On the contrary in the pattern for Cr–V–Mn (4) only a single high peak is observed. This may be interpreted in terms of AF_0 structure.

The diffraction patterns for Cr–V–Mn (1) and (2) are similar to that for Cr–V–Mn (3) corresponding to AF_1 structure and those for Cr–V–Mn (5) and (6) are similar to that for Cr–V–Mn (4) corresponding to AF_0 structure. The temperature dependence of these patterns is

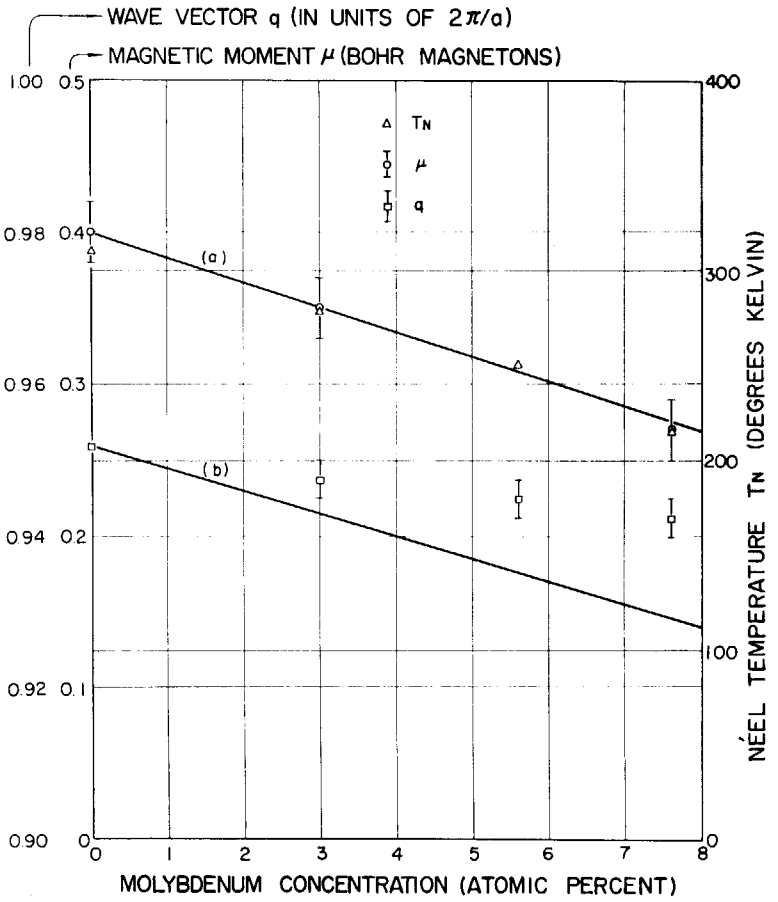

Fig. 14 Concentration dependence of T_N, μ and q for Cr-Mo. Curves (a) and (b) represent μ and q, respectively, for Cr-V having the same T_N as that of Cr-Mo.

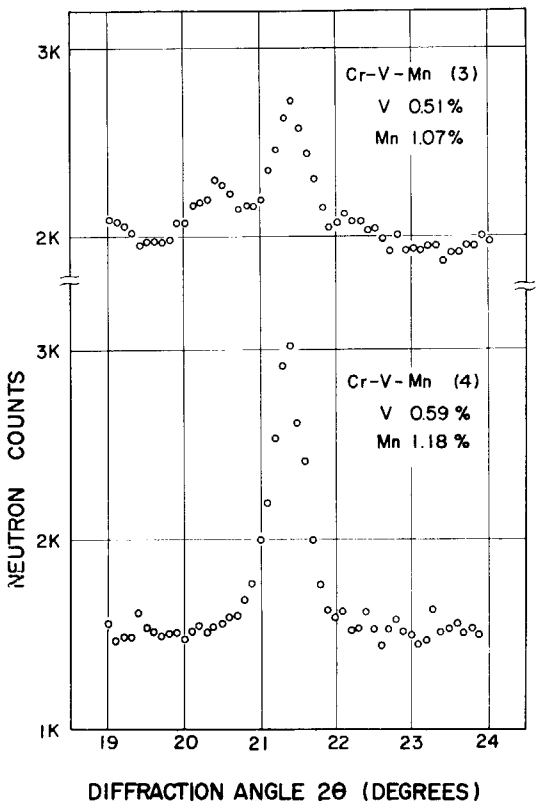

Fig. 15 Diffraction patterns of Cr-V-Mn (3) and (4) at liquid nitrogen temperature

quite simple. With decreasing temperature the patterns do not change in the characteristic way as has been observed in Cr-Mn binary alloy and increases simply according to the Brillouin function with $S=1/2$. The values obtained for the average magnetic moment μ of each specimen are listed in TABLE 1 together with the estimated errors. These are plotted in **Fig. 16** as a function of effective concentration as well as the data on Cr-V and Cr-Mn binary alloys for comparison. As a whole they are on a single curve giving a jump at the effective concentration of 0.6%, where there is a kink in the curve of T_N. Notice that the jump from 0.44 μ_B to 0.65 μ_B may be interpretable by $\sqrt{2}\times 0.44=0.60\ \mu_B$ which is close to 0.65 μ_B, since the jump corresponds to AF_1-AF_0 transition.

For Cr-V-Mn (1), (2) and (3) the values for wave vector q are calculated and listed in TABLE 1 together with the estimated errors. These are plotted in **Fig. 17** as a function of effective

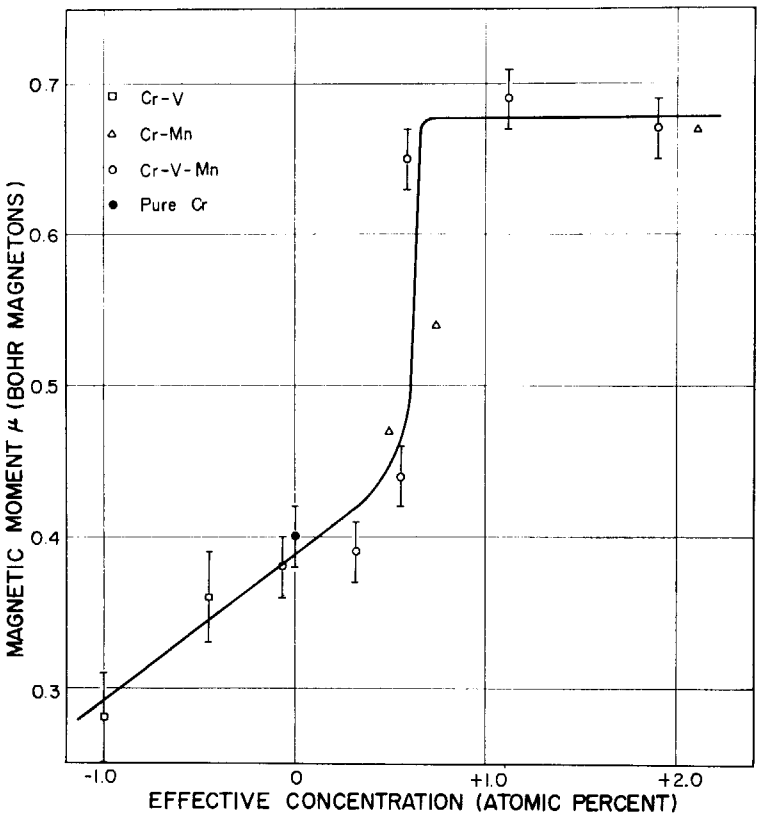

Fig. 16 Concentration dependence of μ for pure Cr, Cr–V, Cr–Mn and Cr–V–Mn alloys

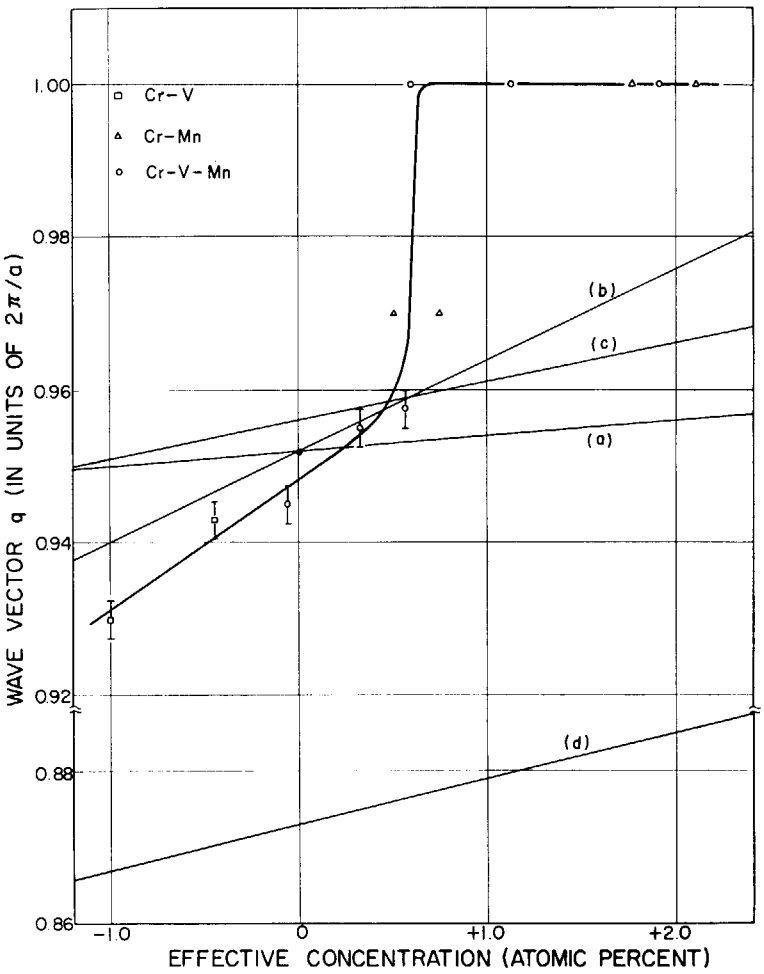

Fig. 17 Concentration dependence of q for pure Cr, Cr–V, Cr–Mn and Cr–V–Mn alloys. Curves (a) and (b) correspond to the values calculated from the single-band model on alternative assumption (a) and (b), respectively. Curves (c) and (d) correspond to those from the two-band model using alternative choice of V_1 and V_2, respectively.

concentration as well as the data on Cr–V and Cr–Mn binary alloys for comparison. On the whole it shows the same trend including a jump at the same effective concentration of 0.6% as in the curve of μ. Notice that the jump from 0.9575 to 1.0000 in units of $2\pi/a$ corresponds to $AF_1 - AF_0$ transition.

The data used above for obtaining μ and q for Cr–V–Mn alloys are all those observed at liquid nitrogen temperature of about 90°K. Since T_N is much higher than the observed temperature in all alloys, the extrapolated values to zero absolute temperature are slightly changed from the values obtained above. However the corrections involved are always smaller than the errors of the quantities.

4.3 Summary of experimental results

All the experimental data are listed in TABLE 1 and plotted as a function of impurity concentration in Fig. 9, 14, 16 and 17. The magnetic phase diagram obtained from our experimental results is shown in Fig. 18 for Cr–V, Cr–Mn and Cr–V–Mn alloy systems. Notice that the phase boundary between AF_1 and AF_0 phases for Cr–V–Mn alloys is slightly different from that for Cr–Mn alloys. The experimental evidence can be summarized as follows.

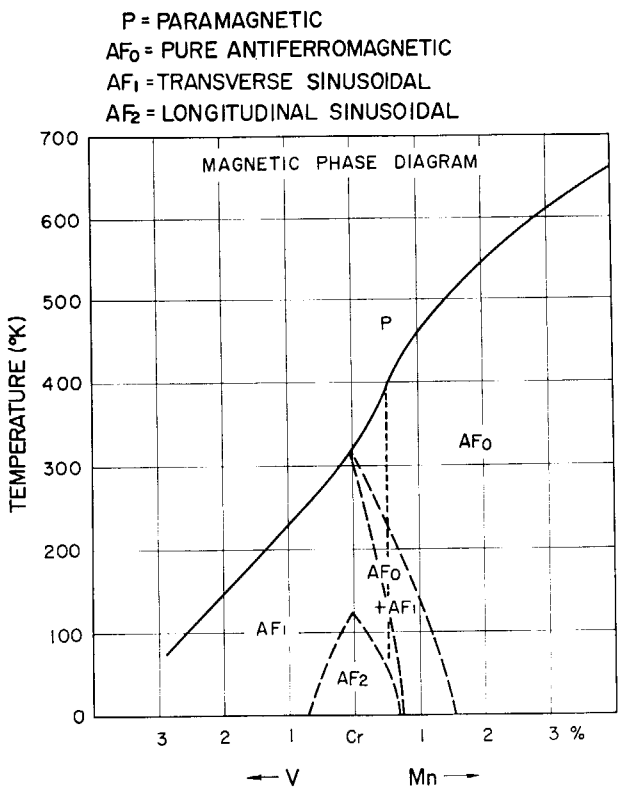

Fig. 18 Magnetic phase diagram for Cr–V, Cr–Mn alloys (full and slashed curves) and for Cr–V–Mn alloys (full and dotted curves)

When V atoms are added to host Cr metal, physical quantities of Cr such as T_N, μ and q of the SDW are decreased rapidly. When Mn atoms are added to host Cr metal, all these physical quantities are increased rapidly up to 5% addition of Mn and then they are increased gradually up to 25 percent. Contrary to Cr–V or Cr–Mn case, the addition of Mo atoms to host Cr metal decreases these physical quantities quite gradually. This fact is especially pronounced for q in Cr–Mo alloys where q remains almost constant.

In Cr–V–Mn ternary alloys these physical quantities as a function of impurity concentrations agree with those for Cr–V or Cr–Mn binary alloys, provided that the comparison is made on the same scale of effective concentration in units of atomic percent in these alloy systems. The kink at 0.6% in T_N–effective concentration curve in Fig. 9 may be compared with the jump in the μ–effective concentration and q–effective concentration curves in Fig. 16 and 17, respectively, at the same effective concentration.

In Cr–Mn alloy with Mn concentration of about 0.6%, a characteristic temperature dependence of μ from AF_0 to AF_1 type with decreasing temperature is observed. In Cr–V–Mn alloys, however, no such temperature dependence could be observed. Insted, a jump from AF_1 to AF_0 structure at 0.6 atomic percent with increasing effective concentration is evidently observed. These experimental facts on Cr–Mn and Cr–V–Mn alloys constitute the main difference

between the two alloy systems.

We notice here the fact that for both binary and ternary alloys the addition of V, Mn or Mo atoms to host Cr metals rapidly develops the tendency to suppress the spin flip transition between AF_1 and AF_2 structure at low temperature. A somewhat analogous situation is also found in Cr-V-Mn in the fact that AF_1 to AF_0 transition with varying temperature is completely suppressed.

5. Discussion of Results

5.1 General remarks on the experimental results

The overall results have established that the magnetic properties of chromium is appreciably influenced by the change in the number of 3d electrons. As has already been stated in **Chapter 1**, we can expect the number of 3d electrons in Cr to be decreased, increased or remains fixed as we add V, Mn or Mo, respectively, to host Cr metal. The magnetic properties of Cr-V-Mn ternary alloys can also be expressed as a unique function of the number of 3d electrons in the same way as in Cr-V or Cr-Mn binary alloys. The presence of about 0.5% V in every Cr-V-Mn specimen is cancelled out with the equivalent amount of Mn. Conseqently only the net concentration of Mn is effective in giving rise to the magnetic properties of the alloys. This is rather surprising from the point of the view that the magnetic properties of Cr is highly sensitive to the addition of other 3d transition metals. This is thougt as a positive, though not decisive, support for the validity of the rigid band approximation in these alloy systems.

Comparing the present results on Cr-Mo with those on the previous Cr-V on the same scale of a physical parameter, we have chosen the μ and q having the same T_N for each alloy system. To do this, we have plotted the curves (a) and (b) in the **Fig. 14** defined as follows. Curve (a) represents the μ for Cr-V having T_N same as that for Cr-Mo of the Mo concentration specified by the curve (a) itself. Curve (b) represents the q for Cr-V having T_N same as that for Cr-Mo of the Mo concentration specified by the curve (b) itself.

As is evident in **Fig. 14**, the curve (a) agrees well with the values of μ for Cr-Mo, while the curve (b) appreciably deviates from the values of q for Cr-Mo. The coincidence of the curve (a) with the μ for Cr-Mo has established that the μ for Cr-Mo decreases proportionally with their T_N as in the case of Cr-V. The disagreement of the curve (b) with the q for Cr-Mo means that the q for Cr-Mo does not change as in the case of Cr-V and remains almost constant. These facts can be thought as an evidence that mechanism for the decrease of these physical quantities in Cr-Mo is quite different from those in Cr-Mo.

From the foregoing discussions, we can point out the following three statements:

a) There is a positive, though not decisive, support for the validity of rigid band approximation in these Cr-V, Cr-Mn and Cr-V-Mn alloy systems.

b) The occurrence of certain types of spin structure in Cr-V, Cr-Mn and Cr-V-Mn alloys has a close correlation with the number of 3d electrons and corresponding Fermi surfaces.

c) In Cr-Mo alloys, where the number of 3d electrons is expected not to be changed, we have to account for the change in the physical properties in terms of different mechanism from that of Cr-V, Cr-Mn and Cr-V-Mn alloys.

The three models which have been proposed to account for the unusual properties of chromium have certain interesting features in the fact that they predict the type of spin structure as a function of the number of 3d electrons. This fact is closely connected with the interrelation between the Fermi surface and the zone boundaries in electron energy bands. Therefore we shall try to interpret the present results in terms of these three models. For this purpose we have described briefly some aspects of these models, separately in **Appendix C.**

5.2 Comparison with the three models

The concentration dependence of the physical quantities should be interpreted in terms of the three kinds of SDW model for chromium. This will provide the test of the validity for each model. However from the existing three models we can calculate only the wave vector of the SDW as a function of effective concentration at zero absolute temperature. Hence hereafter we shall confine ourselves only to the comparison of the theoretical values for q with the experimental values.

Since only MATTHEISS' results[35] are the one from which we are able to get the energy–wave vector curve of the bands in certain symmetry directions in the Cr group metals, we shall exclusively make use of his results hereafter in the interpretation of our present results. In **Fig. 19** we reproduce a part of his results on the energy–wave vector curve in (100) direc-

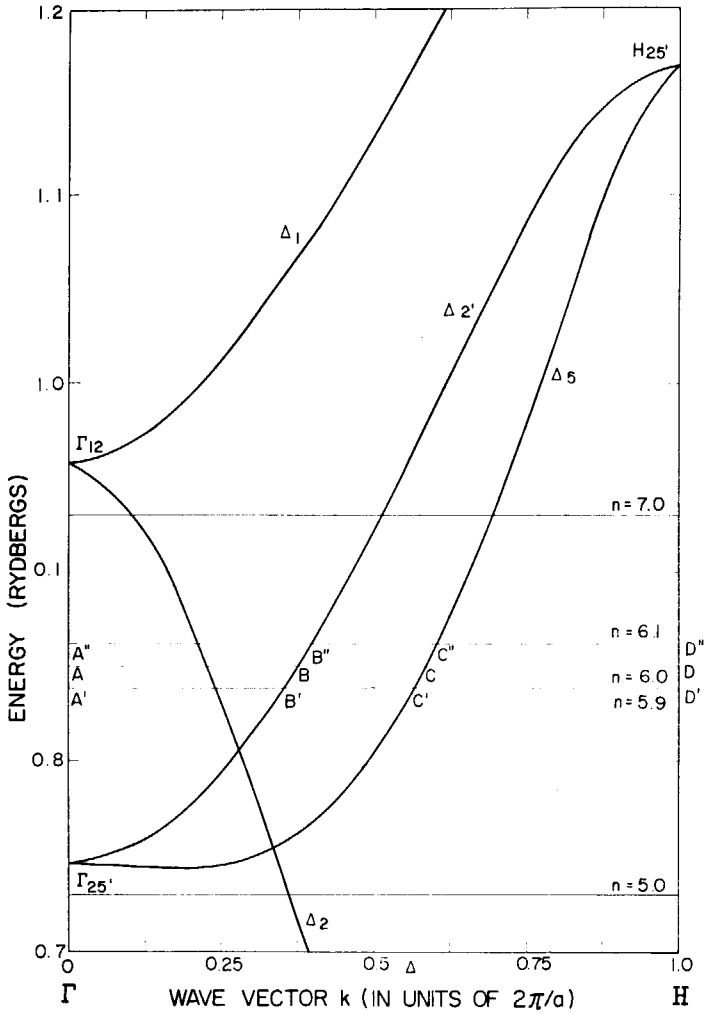

Fig. 19 Reproduction of (100) direction of band structure for Cr group metal using atomic potential V_1 after MATTHEISS. Fermi level for Cr is indicated by ABCD.

tion[35] for HARTREE-FOCK-SLATER atomic potential $V_1(r)$. He has also obtained the similar curves for a slightly different potential $V_2(r)$, in which the exchange potential in $V_1(r)$ is reduced by 30%. For Cr the number (n=6) of 3d and 4s electrons corresponds to the Fermi surface indicated by ABCD in Fig. 19. Since MATTHEISS has given a density of state curve as a function of Fermi energy, we are able to know the Fermi energy as a function of electron number. Therefore assuming a rigid band approximation, the addition of 10 atomic percent V to Cr results in the electron number $n=5.9$ corresponding to the Fermi surface at A'B'C'D' and similarly the addition of 10 atomic percent Mn to Cr results in $n=6.1$ corresponding to the Fermi surface at A″B″C″D″. The Fermi surface in (100) plane according to the calculation by MATTHEISS[35] is shown in Fig. 20, in which the points A, B, C and D corresponds exactly to those in Fig. 19. In the following we shall discuss the behavior of q as a function of electron number according to each of the three models on the basis of the rigid band approximation.

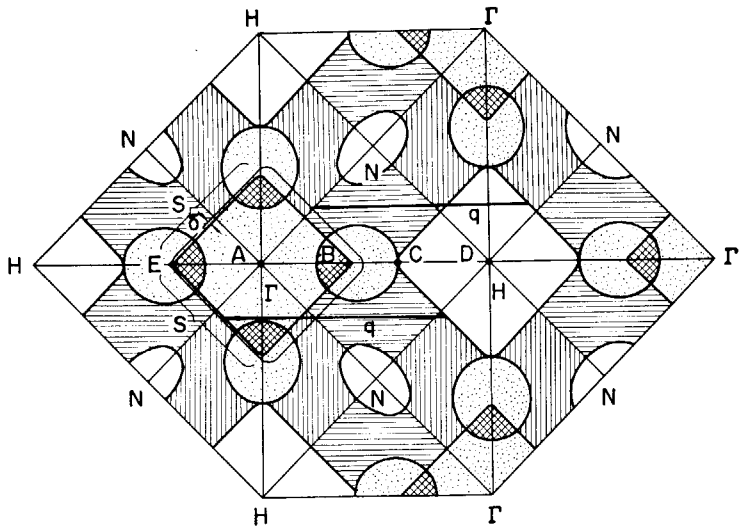

Fig. 20 Fermi surface in (100) plane in Cr using atomic potential V_1 after MATTHEISS. A hole octahedron around H is shifted toward an electron jacket around Γ by the vector q slightly smaller than 1 so as to give a large contact area S and small average separation δ.

5.2.1 Free electron model by OVERHAUSER[27]

According to this model, q is given by (c. 12)

$$q=2k_F \qquad (1)$$

where k_F is the wave vector of the free electrons at Fermi surface. In the light of band structure, the free electrons may be approximated by the electrons at either Δ_2' or Δ_5 branch of the band structure in Fig. 19. Thus we can choose as $q=2$ AB or 2 AC. Since 2 AC is greater than unity for both V_1 and V_2, the choice of 2 AC for q is rejected. Thus for q we shall use exclusively 2 AB for pure Cr, 2 A'B' for 10% addition of V and 2 A″B″ for 10% addition of Mn. Thus we can calculate the values for q for Cr and Δq/percent defined as the change in q per 1 atomic percent change in concentration for both V_1 and V_2, respectively. These are listed in TABLE 2. However they can not be shown in Fig. 17, because they are too small.

5.2.2 Single-band model by TACHIKI and NAGAMIYA

According to their numerical calculation and the analysis made by the present author in the paper[21], q can be expressed in units of $2\pi/a$ by the formula

$$q_0 - q = \xi(n_0^{1/3} - n^{1/3}) \qquad (2)$$

where $q_0 = 0.9546$ and $n_0 = 0.5007$ and $\xi = 2.25$ are the numerical constants. For pure chromium the set of values $q = 0.952$, $n = 0.4985$ is to be satisfied. We calculated the changes in the electron number by two alternative assumptions; (a) the addition of vanadium (or manganese) acts to decrease (or increase) the the number of 3d electrons uniformly in all of the five degenerate bands, (b) the changes in the electron number take place only in the single band which is responsible for the occurrence of SDW. The addition of 1 atomic percent of V or Mn should change the electron number by 0.002 on the assumption (a) and 0.01 on the assumption (b), respectively[42]. The values for q and Δq/percent thus determined are listed in TABLE 2 and plotted in Fig. 17 with the marks (a) and (b). The coincidence of the calculated values of 0.952 for q for chromium with the experimental value is a natural consequence of the choice of the electron number as an adjustable parameter. Thus we should notice only the gradient Δq/percent for the test of the theory. Perhaps the real situation with respect to the change in electron number must lie between the two extreme assumptions.

TABLE 2. Calculated values for the wave vector q (in units of $2\pi/a$) and the gradient of q with respect to the concentration Δq/percent (in units of $2\pi/a$ per 1%) from the three models for Cr together with the experimental values. V_1 and V_2 show two alternative choices of atomic potential. (a) and (b) show two extreme alternative assumptions on the rate of changes in electron number. The truth must lie between (a) and (b).

	OVERHAUSER		TACHIKI & NAGAMIYA		LOMER		Experimental
	V_1	V_2	(a)	(b)	V_1	V_2	
q	0.750	0.600	0.952	0.952	0.956	0.873	0.952
Δq/percent	0.005	0.008	0.002	0.012	0.005	0.006	0.020

5.2.3 Two-band model by LOMER[30]

As has been pointed out at first by LOMER and later discussed by FEDDERS and MARTIN[31], the most plausible wave vector q along (100) axis of SDW in chromium is such that [See (c. 20)] at which

$$S \ln(\pi/2\delta) \qquad (3)$$

becomes maximum, where S is the area of close contact of the Fermi surfaces of two bands and δ is an average separation between the two surfaces as shown in Fig. 20. In this case the two bands correspond to the electron jacket around the symmetry point Γ and the hole octahedron around H. However it is quite difficult to find out a correct value for q, since in the criterion for q the δ should be considered in three dimensions. For simplicity we approximate as

$$q = \mathrm{EC} = \mathrm{AB} + \mathrm{AC} \qquad (4)$$

in Fig. 20 connecting the Fermi surfaces of two bands along the (100) axis. We then obtain the approximate values for q and Δq/percent, again taking into account the change in Fermi surface as shown in Fig. 19 in the same manner as for the free electron model. The results for both V_1 and V_2 are also included in TABLE 2 and plotted in Fig. 17 with the marks (c) and (d), respectively. Although the curve (d) is far below the experimental values, the gradient of the curve, i.e. Δq/percent is same as that for the curve (c). This shows that the absolute value for q is quite sensitive to the choice of atomic potential, while its gradient is not.

The results on the concentration dependence of q are plotted in Fig. 17 and summarized in TABLE 2. This shows the gradient of q with respect to the concentration, i.e. Δq/percent, has the same order of magnitude of 0.005 for all the three models which is 4 times smaller than the experimental value of 0.020. Such circumstances indicate that these three models can well explain the tendency of q as a function of electron number qualitatively, but not quantitatively.

There have been certain approximations employed in the calculation of the values for q from the three models. We have approximated the free elecrons to be on the Δ_2' branch of the band structure in the model (a), assumed the Fermi surface to be spherical in the model (b) and considered the shape of the Fermi surface only along the (100) direction in the model (c). Another approximation lies in the fact that the experimental values for q obtained from the data at liquid nitrogen temperature were compared with the theoretical ones at absolute zero temperature in the model (a) and (c) and the theoretical one at Néel temperature in the model (b). To get more definite conclusions about the validity of the models, we should improve the approximations along this line.

5.2.4 Situation in Cr-Mo alloys

The fact that in Cr–Mo alloys the q remains almost constant while other physical quantities such as T_N and μ decrease gradually assures that the situation in Cr–Mo alloys is quite different from that encountered in Cr–V, Cr–Mn and Cr–V–Mn alloy systems. Since the addition of Mo into Cr melal is thought not to change the number of d-electrons, the constancy of q can be explained in either of the three models discussed above. Therefore the change in T_N and μ in Cr–Mo alloys should be interpreted in a different way from the other alloy systems in terms of single-band and two-band models.

According to the calculation by MITSUDO et al[43] on the basis of the single-band model a small increase in U, intra-atomic coulomb integral in the same band, results in a decrease in T_N, while this does not affect much the values of q determined from the maximum of U^{-1}–q curve. Thus although we have very little knowledge on the values for U, we can give an interpretation that in Cr–Mo alloys U increases with addition of Mo giving rise to a decrease in T_N in the single-band model (b).

According to the two-band model a linear relationship between μ and T_N is proposed as in (c. 23). This has been verified experimentally on Cr–Mo alloys as shown in Fig. 14. The formulas (c. 21) and (c. 22) predict that T_N is dependent on the overlap integral γ in the same band, while several other factors relating with the shape of the two bands are unchanged in Cr–Mo alloys. Therefore, within the framework of the two-band model, the gradual decrease in T_N and μ in Cr–Mo alloys can be interpreted in terms of the change in γ.

The above discussions show that although both the single-band and two-band models are able to interpret the experimental evidence in Cr–Mo alloys, the two band model is more flexible in interpretation than the single-band model.

5.3 Relation of Fermi surface to energy gap

In the previous discussion we have established the validity of rigid band approximation and have shown a possible explanation of the experimental results on neutron diffraction in terms of three kinds of model for chromium. The comparison among the three models has made it apparent that none of them is decisively superior to the other two. However, a consideration

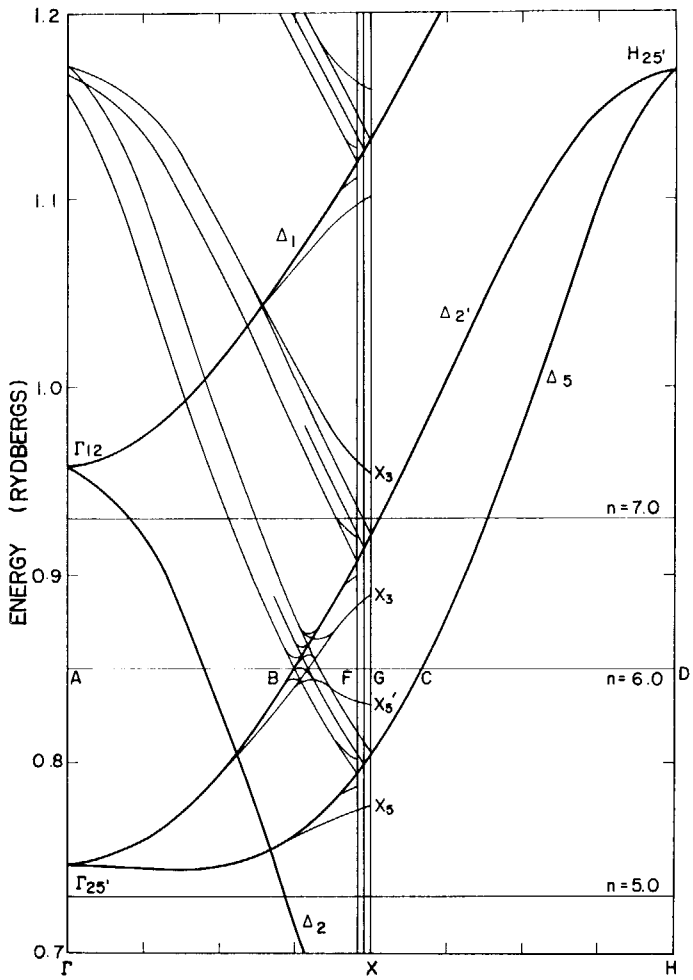

Fig. 21 Incommensurable and commensurable split-band structure in Cr represented schematically. Due to an energetic advantage at the energy gap B, commensurable structure is more stable than incommensurable one.

on the behavior in electrical resistivity together with the concentration dependence of magnetic structure in Cr-V-Mn, i. e. AF_0-AF_1 transition will distinctly favor the two-band model.

In **Fig. 21** we give a slightly modified band structure of original one as given in **Fig. 19**. A SDW state with AF_1 structure in Cr has an incommensurable zone boundary at the middle position F between B and C. The position F is slightly toward left as compared with the commensurable zone boundary at the point G. The Δ_5 branch is reversed symmetrically with respect to F, thus connecting C to B. Both the Δ_5 and Δ_2' branch will split into lower and upper parts, respectively, along the vertical line through F. The formation of AF_1 structure will also produce another new energy gap at B as a result of mixing of electrons on the band Δ_2' and Δ_5. Strictly speaking this mixing does not occur in the neighbourhood of (100) symmetry direction, but does occur in the direction deviated from the (100) symmetry direction. Therefore the representation in **Fig. 21** is not correct and should be taken only schematically. This energy gap will, in turn, truncate the Fermi surface of the band Δ_2' and Δ_5. As the number of electrons is increased, the position of energy gap will shift toward right, until an incommensurable energy gap at F disappears and at the same time a commensurable one at G appears. This change from incommensurable to commensurable structure takes place abruptly at a certain electron concentration. This is because the commensurable structure has a certain energetic advantage as compared with the incommensurable one.

According to the calculation by ASANO[44] on the energy band for Cr having a pure antiferromagnetic super-structure, a fairly large splitting appears at the commensurable zone boundary. The magnitude of the splitting is expected to be twice that of the incommensurable one, since the average magnetic moment in commensurable structure is $\sqrt{2}$ times larger than that in incommensurable one. The perturbation due to the formation of commenstrable structure also modifies the energy gap at B. The magnitude of the splitting is again twice that of the incommensurable one. Therefore the onset of AF_0 structure will decrease the total energy on the lower branch below the energy gap at B. Thus the energy of the whole system in AF_0 state becomes less than that in AF_1 state at certain electron concentration.

As the number of electrons increases further, the AF_0 structure persists. However, the fraction of truncation in Fermi surface will become larger as the number of electrons increases. This explains the temperature dependence of electrical resistivity in Cr-Mn and Cr-V-Mn in AF_0 region, in which the resistivity increase at lower temperature becomes larger with increasing effective concentration. The similar behavior in resistivity is reported for Cr-Fe alloys in AF_0 region[45][46]. This behavior in Cr-Fe can also be interpreted in the same manner as in Cr-Mn and Cr-V-Mn alloys.

The well known HUME-ROTHERY[47] rule was the first to correlate the type of crystal structure with the Fermi surface. The position of the Fermi surface with respect to the energy zones determines the crystal structure to be stabilized. YOSIDA and WATABE[48] has extended this idea in explaining the magnetic structure to be stabilized in rare earth metals. The screw structure in rare earth metals is stable due to the formation of new energy gap touching the Fermi surface.

The present interpretation on AF_1 to AF_0 transition in Cr-Mn and Cr-V-Mn alloys in terms of an increase in electron number is a new version of the idea originating from HUME-ROTHERY. The similar interpretation on the occurrence of pure antiferromagnetism in metals and alloys may be applied to other substances, for instance, Cr-Fe alloys and pure Mn metal.

6. Conclusion

6.1 Concluding remarks

The various conclusions deduced from the previous discussions in line with the problems in **Chapter 1**, are following :

1) The rigid band approximation has proved to be fairly good in understanding the properties of various chromium alloys. Incommensurable-to-commensurable transition as a function of electron concentration is not a failure of this approximation, but gives a support for the extention of the idea developed by HUME-ROTHERY and by YOSIDA and WATABE to understanding a stability condition for pure antiferromagnetic structures in metals.
2) The various properties of chromium and its alloys with other transition metals are explicable in terms of either of the three models. However the two-band model is the most flexible among them and therefore provides the most promising basis for future studies.
3) The concept of itinerant antiferromagnetism has now been almost established in understanding the behavior in the magnetic properties of chromium and its alloys. The concept of itinerant antiferromagnetism owes much to SDW theory developed by OVERHAUSER.

In addition to this the concept of Fermi surface has proved to be a very useful tool in analyzing the experimental results.

6.2 Prospects for future studies

Traditionally magnetic behaviors in transition metals and alloys are so complicated that the investigations performed on them by various authors have been very much controversial up to the present. However we can say at this stage that we have found a clue for understanding itinerant antiferromagnetism in metals and alloys, i. e. a SDW theory, and also found some useful tools for further investigation. These tools are :

1) rigid band approximation
2) concept of Fermi surface
3) extended Hume-Rothery rule.

Using these tools further experimental studies should be pursued in the future to get informations on the various properties of transition metals and alloys. Neutron diffraction studies, including both elastic and inelastic scattering, will provide very useful means of investigation along this line.

A possible itinerant ferro- or antiferromagnetism in various 3d-transition metal alloys including Cr, Mn, Fe, Co and Ni should be investigated in more detail. It is suggested that a theory of electrical resistivity for itinerant antiferromagnetic metals should be formulated according to the proposed mechanism which accounts for the incommensurable-to-commensurable transition in this paper.

Acknowledgements

The author wishes to express his sincere appreciation to Prof. Y. TOMONO for guiding me to prepare this thesis. The author is pleased to acknowledge the constant help and advice of Prof. N. KUNITOMI and Dr. Y. HAMAGUCHI throughout the every stage of this investigation.

The author is greatly indebted to Dr. H. HASHITANI and Mr. K. KATSUYAMA in the analytical chemistry laboratory in JAERI for the chemical analysis of the specimens, without whose help this investigation would be impossible. The author is also grateful to Mr. N. MINAKAWA in our laboratory for his technical assistance during the course of the neutron diffraction experiments.

The author has been profited through stimulating discussion with Drs. Y. OBATA and K. SASAKI. The author is grateful to my colleagues Dr. M. SAKAMOTO and Mr. H. MOTOHASHI for their help whenever it was needed.

Appendix A. Transport properties in oscillatory magnetic structures

The theory of electrical resistivity in rare earth metals having screw-type spin arrangement has been developed by MIWA[49] and ELLIOTT and WEDGWOOD[50]. The electrical resistivity in chromium having sinusoidal spin arrangement can also be interpreted essentially in terms of the same formula as in rare earth metals.

These authors have obtained the temperature dependence of the electrical resistivity as

$$\rho(T) = \frac{\rho_i + \rho_l(T) + \rho_m(T)}{1 - g m_{osc}(T)} \qquad \text{(a. 1)}$$

where ρ_i is the resistivity due to impurity scattering, which is temperature independent, $\rho_l(T)$ is that due to the lattice scattering which is proportional to T^5 at low temperature and proportional to T at high temperature, $\rho_m(T)$ is that due to the spin disorder scattering via s-d exchange interaction and is proportional to $1-\frac{M(T)^2}{M(O)^2}$, where the magnetization $M(T)$ varies with temperature according to the Brillouin function, g is a constant, $m_{osc}(T)$ means a fraction of the reduction in the effective number of conduction electrons due to the truncation of Fermi surface by the energy gap in the electron bands. This fraction $m_{osc}(T)$ is proportional to $M(T)$.

As a result of these several factors, i. e. ρ_i, $\rho_l(T)$, $\rho_m(T)$, $1-gm_{osc}(T)$ as represented in **Fig. 22** (a) (b) and (c), the temperature dependence of the electrical resistivity $\rho(T)$ as given by (a. 1) can be represented as in **Fig. 22** (d). The temperature at which the minimum of the resistivity occurs corresponds exactly to the Néel temperature T_N.

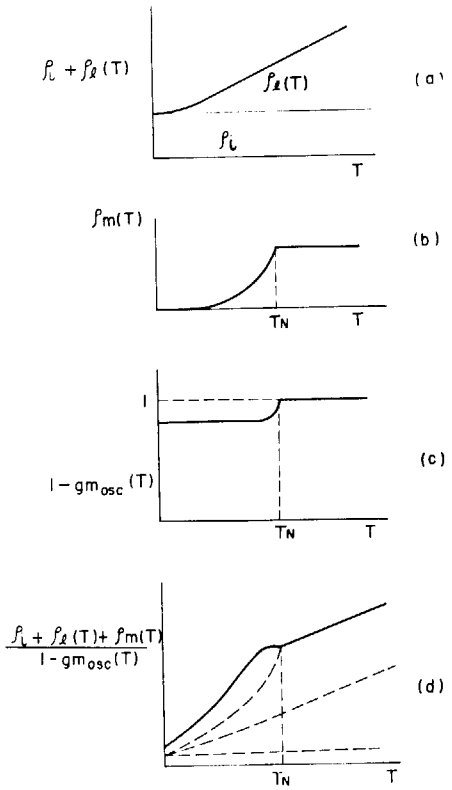

Fig. 22 Schematic representation of various factors determining the electrical resistivity in oscillatory structure. Combination of (a), (b) and (c) results in (d).

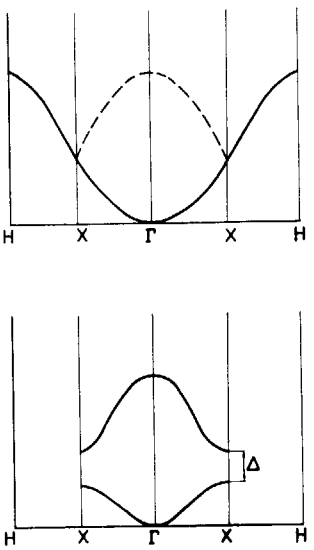

Fig. 23 Schematic representation of split-band model for antiferromagnetism

No one has ever formulated the electrical resistivity in antiferromagnetic metals and alloys. According to the split-band model originally proposed by SLATER[51] and later elaborated by MATSUBARA and YOKOTA[52], the formation of antiferromagnetism results in a splitting of a band, as the band at the top of **Fig. 23** splits into two bands in a half-zone as at the bottom of **Fig. 23**. The energy splitting Δ between the upper and lower band can be determined self-consistently. Such a splitting Δ should certainly manifests itself in the transport phenomena like the energy gap in oscillatory magnetic structures. Therefore we can expect resistivity minimum in antiferromagnetic metals and alloys as given by (a. 1). However in the two band model by LOMER[30], the mechanism which produces a splitting in antiferromagnetic structure is slightly different from the simple spit-band model described above. For this two-band model, the reader is referred to the **Chapter 5** of the present thesis.

These behaviors in the temperature dependence of the electrical resistivity make it possible to determine the Néel temperature in the Cr-based binary or ternary alloy systems, as far as they have sinusoidal spin structure or antiferromagnetic structure.

Appendix B. Fundamentals of magnetic scattering of neutrons

The scattering of neutrons from materials having atomic magnetic moment arises mainly from two sources ; 1) nuclear interaction between neutrons and neulei in the materials via short range nuclear forces, 2) magnetic dipole-dipole interaction between the magnetic moment of neutrons and the magnetic moment of the atomic electrons in the materials.

Nuclear scattering of neutrons from an atom is simply expressed in terms of only isotropic s-wave. The differential cross section through solid angle $d\Omega$ from an atom is given by

$$\frac{d\sigma}{d\Omega}=b^2, \tag{b. 1}$$

where b is nuclear scattering amplitude originally proposed by FERMI[53]. The values for b can be determined experimentally and are now obtainable from the most standard text books.

The theory of magnetic scattering of neutrons was first developed by HALPERN and JOHNSON[54]. The differential cross section through solid angle $d\Omega$ from an atom is dependent on the relative orientation of scattering vector to the direction of magnetic moment of the atom. Magnetic scattering of neutron from an atom having electronic magnetic moment is given by

$$\frac{d\sigma}{d\Omega}=(r_0\gamma)^2S^2f^2(\vec{K})\vec{q}^2, \tag{b. 2}$$

where $r_0=\dfrac{e^2}{mc^2}$ is the classical electron radius, $\gamma=-1.913$ is the value for the magnetic moment of neutrons in units of nuclear magneton, S is the spin of the atom, $f(\vec{K})$ is the magnetic form factor of the atom which can be expressed in terms of the density distribution of magnetic electrons $\rho(\vec{r})$ by

$$f(\vec{K})=\int_{\text{atom}}\exp(i\vec{K}\vec{r})\rho(\vec{r})d\vec{r},$$

where scattering vector $\vec{K}=\vec{k}_0-\vec{k}'$, i. e. the difference between the wave vector of the incident and scattered neutrons, $\vec{q}$ is given by

$$\vec{q}=\vec{e}(\vec{e}\cdot\vec{\kappa})-\vec{\kappa}$$

where $\vec{e}$ is the unit scattering vector and $\vec{\kappa}$ a unit vector parallel to the magnetic moment

vector of the atom. If we put $p=r_0\gamma Sf(\vec{K})$, then

$$\frac{d\sigma}{d\Omega}=p^2\vec{q}^2, \tag{b. 2'}$$

where p may be called magnetic scattering amplitude. Note that the sign of p is determined by S. The value for S may be plus or minus according as the direction of the magnetic moment of the atom is either parallel or antiparallel to the sublattice magnetization axis in an antiferromagnet.

The combination of nuclear and magnetic scattering results in the differential cross section for unpolarized neutrons as follows;

$$\frac{d\sigma}{d\Omega}=b^2+p^2\vec{q}^2, \tag{b. 3}$$

The total differential scattering cross section through solid angle $d\Omega$ from atoms in the lattice for unpolarized neutrons can be expressed by

$$\left(\frac{d\sigma}{d\Omega}\right)_{\text{tot}}=\left|\sum_{\substack{\text{all}\\ \text{atoms}}} b_j\exp(i\vec{K}\vec{r}_j)\right|^2+\left|\sum_{\substack{\text{all}\\ \text{atoms}}} p_j\vec{q}_j\exp(i\vec{K}\vec{r}_j)\right|^2. \tag{b. 4}$$

The summation should be taken for all atoms in the lattice. b_j and p_j are nuclear and magnetic scattering amplitude for j-th atom. $\vec{q}_j$ and $\vec{r}_j$ refer also to j-th atom. We put

$$\vec{r}_j=\vec{r}_L+\vec{r}_m, \tag{b. 5}$$

where $\vec{r}_L$ is the position vector of L-th unit cell and $\vec{r}_m$ the position vector of m-th atom in the unit cell. Carrying out the summation over L and m separately, we finally get for nuclear scattering

$$\left(\frac{d\sigma}{d\Omega}\right)_{\text{nucl}}=\frac{(2\pi)^3N_c}{V_c}b^2\left|\sum_m e^{i\vec{K}\vec{r}_m}\right|^2\sum_{\vec{G}}\delta(\vec{K}-\vec{G}) \tag{b. 6}$$

and for magnetic scattering

$$\left(\frac{d\sigma}{d\Omega}\right)_{\text{mag}}=\frac{(2\pi)^3N_c}{V_c}(r_0\gamma)^2f^2(\vec{K})S^2\{1-(\vec{e}\cdot\vec{\kappa})^2\}\left|\sum_m e^{i(\vec{K}\vec{r}_m+\phi_m)}\right|^2\sum_{\vec{G}}\delta(\vec{K}-\vec{G}), \tag{b. 7}$$

where N_c is the total number of unit cell, V_c is the volume of unit cell, $\vec{G}$ is reciprocal lattice vector of simple cubic structure, $\left|\sum_m e^{i\vec{K}\vec{r}_m}\right|^2$ and $\left|\sum_m e^{i(\vec{K}\vec{r}_m+\phi_m)}\right|^2$ refer to nuclear and magnetic structure factor, respectively, and ϕ_m is the phase of the magnetic moment of m-th atom in the unit cell.

The formula (b. 6) shows that nuclear Bragg peaks appear at the same position as in X ray Bragg peaks determined by the structure factor $\left|\sum_m e^{i\vec{K}\vec{r}_m}\right|^2$, The formula (b. 7) shows that since in a ferromagnet $\phi_m=0$ magnetic coherent peaks appear at the same position as the nuclear Bragg peaks. In an antiferromagnet, the position of magnetic coherent peaks is determined by the magnetic structure factor $\left|\sum e^{i(\vec{K}\vec{r}_m+\phi_m)}\right|^2$ and therefore does not generally coincides with the nuclear coherent peaks.

In an antiferromagnet a comparison of magnetic scattering intensities to nuclear scattering intensities makes it possible to determine the magnetic scattering amplitude p, provided the value for nuclear scattering amplitude b is known. Hence we can determine the value of magnetic moment.

In the case of oscillatory magnetic structures[55),56)], we difine a wave vector $\vec{\tau}$ which characterizes the oscillatory modulation to be considered, for instance, a transverse sinusoidal structure. We choose here a nomenclature $\vec{\tau}$ instead of $\vec{q}$ in order to avoid the confusion between the wave vector of SDW and $\vec{e}(\vec{e}\cdot\vec{\kappa})-\vec{\kappa}$. In the rest of this **Appendix B** the nomenclature $\vec{\tau}$ is used for the wave vector of SDW throughout.

We denote the spin of m-th atom in the L-th unit cell by S_m^L. The transverse sinusoidal

structure with wave vector $\vec{\tau}$ parallel to the z axis is expressed in the form

$$\vec{S}_m^L = S\cos(\vec{\tau}\vec{r}_L+\phi_m) = \frac{S}{2}\left[e^{i(\vec{\tau}\vec{r}_L+\phi_m)}+e^{-i(\vec{\tau}\vec{r}_L+\phi_m)}\right]. \tag{b. 8}$$

Then the magnetic scattering intensities are expressed by

$$\frac{d\sigma}{d\Omega} = \frac{(2\pi)^3 N_c}{V_c}(r_0\gamma)^2 f^2 S^2 \frac{1-(\vec{e}\cdot\vec{\kappa})^2}{4}\left[\left|\sum_m e^{i(\vec{K}\vec{r}_m+\phi_m)}\right|^2 \sum_{\vec{G}}\delta(\vec{K}+\vec{\tau}-\vec{G}) + \left|\sum_m e^{i(\vec{K}\vec{r}_m-\phi_m)}\right|^2 \sum_{\vec{G}}\delta(\vec{K}-\vec{\tau}-\vec{G})\right]. \tag{b. 9}$$

Thus the magnetic scattering from oscillatory magnetic structure manifest itself in two equally spaced satellites of the magnetic reflecions allowed by the magnetic structure factor. The magnitude of separation is simply $\pm\tau$. When τ is expressed in units of $2\pi/a$, the inverse of τ gives the spacial period of the oscillatory modulation in unit cells.

Comparison between the formulas (b. 7) and (b. 9) indicates that when the antiferromagnetic structure changes into an oscillatory structure, the integrated intensity reduces to half the original value due to the presence of factor 1/4 and two terms in (b. 9).

The criterion for appearance or disappearance of every satellite peak is again given by the magnetic structure factor. The appearance of nuclear or ferromagnetic coherent peaks, antiferromagnetic coherent peaks and antiferromagnetic satellite peaks is determined as in **Fig. 24** in terms of nuclear or magnetic structure factor multiplied by Laue's diffraction function expressed as $\sum_{\vec{G}}\delta(\vec{K}-\vec{G})$ or $\sum_{\vec{G}}\delta(\vec{K}\pm\vec{\tau}-\vec{G})$ for bcc structure.

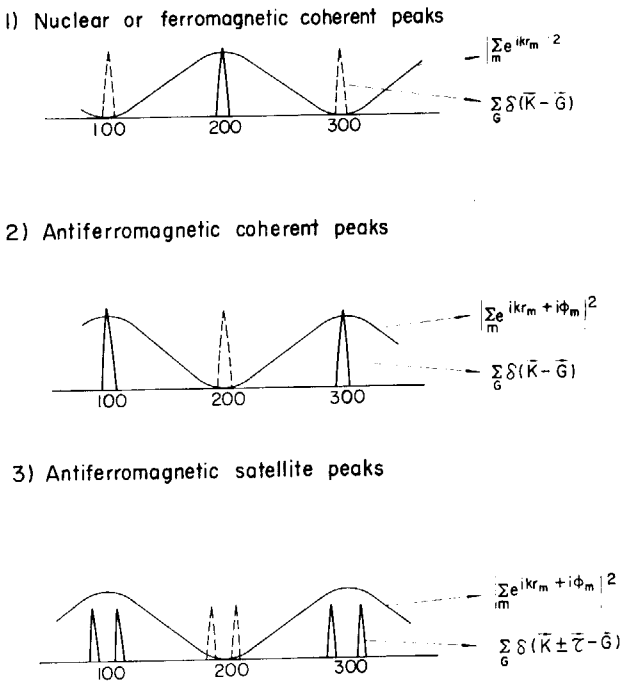

Fig. 24 Criterion for appearance or disappearance of various peaks as determined by the structure factor multiplied by Laue's function

Hitherto we heve considered only a single crystal having single magnetic domain. In the case of polycrystal having three kinds of magnetic domain in which the direction of magnetic moment is aligned parallel to one of the cube axes, the total scattering intensities should be determined by taking into account the factor $\vec{q}^2 = 1-(\vec{e}\cdot\vec{\kappa})^2$ in three dimensions. A simple calcu-

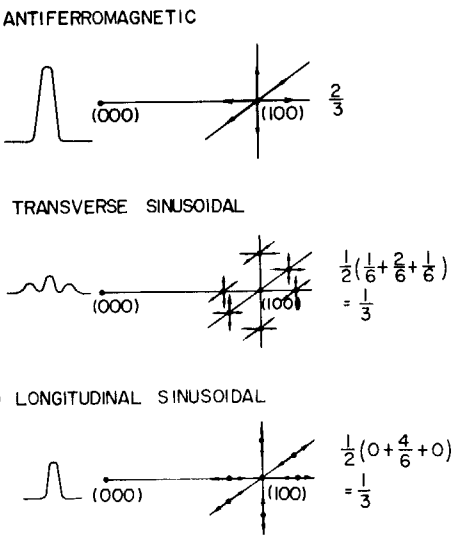

Fig. 25 Intensity consideration for three types of magnetic structures in powder diffraction patterns using unpolarized neutron

lation shows that in ferro- or antiferromagnetic polycrystals having bcc structure a θ-2θ drive measurement gives rise to a single peak at (200) or (100), respectively, and the $\vec{q}^2$ factor is 2/3. In transverse sinusoidal structure the peak is further split into three peaks: two side peaks corresponding to $(1-\delta,\ 0,\ 0)$ and $(1+\delta,\ 0,\ 0)$ reflection and a single central peak including $(1,\ \pm\delta,\ 0)$ and $(1,\ 0,\ \pm\delta)$ reflections. The corresponding intensities of the three peaks are 1/6, 2/6 and 1/6, respectively, and in all $\vec{q}^2$ factor is again 2/3. In longitudinal sinusoidal structure the same measurement gives rise to a single peak including $(1\pm\delta,\ 0,\ 0)$, $(1,\ \pm\delta,\ 0)$ and $(1,0,\ \pm\delta)$ reflections and the $\vec{q}^2$ factor remains unchanged being 2/3. The above simple calculation combined with the consideration that the scattering intensity from oscillatory structure is half that of pure antiferromagnetic structure results in the relative intensities of various peaks in the three types of structure as illustrated in **Fig. 25** for bcc structure.

Appendix C. Three models for chromium

C.1 free electron model by OVERHAUSER[27]

Consider states of a free electron gas which have a net fractional spin polarization $\vec{S}(\vec{r})$ at every point, but with the derection of $\vec{S}$ varying with position as in a spiral SDW:

$$\vec{S}(\vec{r})=S(\vec{x}\cos qz+\vec{y}\sin qz). \tag{c. 1}$$

The axis of q of the SDW is taken here to be the z direction, which is perpendicular to the plane of polarization defined by the unit vectors $\vec{x}$ and $\vec{y}$.

A spin polarization of the form (c. 1) leads to an off diagonal contribution A'' to the one electron exchange potential $A\equiv A'+A''$,

$$A=A'-g\vec{\sigma}(\vec{x}\cos qz+\vec{y}\sin qz) \tag{c. 2}$$

where $\vec{\sigma}$ is the Pauli spin operator. A' is the diagonal part of the one electron exchange energy. The amplitude g of the off diagonal contribution will, in general, be dependent on the wave vector of the electron considered. If the spin operators are substituted explicitly,

$$A''=-g\begin{pmatrix} 0 & e^{-iqz} \\ e^{iqz} & 0 \end{pmatrix}. \tag{c. 3}$$

The operator A'' connects plane wave states in pairs:

$$\vec{k},\ \alpha \rightleftharpoons \vec{k}+\vec{q},\ \beta, \tag{c. 4}$$

where α and β are the spin-up and spin-down spin functions. Consequently HARTREE-FOCK equation

$$\left[\frac{p^2}{2m}+A\right]\Psi=E\Psi \tag{c. 5}$$

can be solved formally. The eigenvalues are those of a two dimensional secular equation:

$$E_k=\frac{1}{2}(\varepsilon_{\vec{k}}+\varepsilon_{\vec{k}+\vec{q}})\pm\left[\frac{1}{4}(\varepsilon_{\vec{k}}-\varepsilon_{\vec{k}+\vec{q}})^2+g^2)\right]^{\frac{1}{2}} \tag{c. 6}$$

The one electron energy $\varepsilon_{\vec{k}}$ is the free electron energy plus the diagonal part A' of the one-electron exchange energy. The two branches of the eigenvalue spectrum are shown in **Fig. 26**. The exact wave functions for the lower branch are

$$\varphi_k=\frac{1}{\sqrt{V}}\left\{\alpha\cos\theta e^{i\vec{k}\vec{r}}+\beta\sin\theta e^{i(\vec{k}+\vec{q})\vec{r}}\right\}, \tag{c. 7}$$

where

$$\cos\theta(\vec{k})\equiv\frac{g}{\left[g^2+(\varepsilon_{\vec{k}}-E_{\vec{k}})^2\right]^{\frac{1}{2}}}. \tag{c. 8}$$

The algebraic signs have been defined as

$$0\leqq\theta\leqq\frac{1}{2}\pi, \tag{c. 9}$$

so that the wave function (c. 7) refer to the lower branch in **Fig. 26**. The factors $\cos\theta$ and $\sin\theta$ define the fraction of mixing of either α or β spin functions.

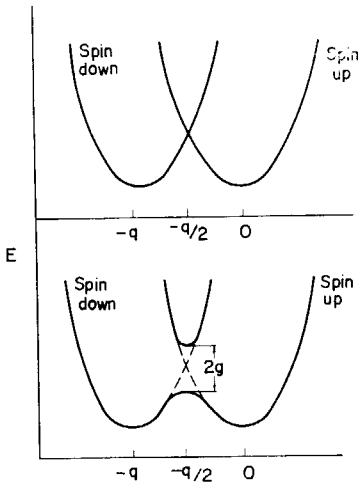

Fig. 26 Single-particle energy level spectrum for spiral SDW. The spin-down branch has been displaced by q to the left of the spin-up branch by virtue of exchange potential.

OVERHAUSER has obtained a self-consistent integral equation for $g(k)$:

$$g(\vec{k}')=\int\frac{4\pi e^2}{|\vec{k}'-\vec{k}|^2}\sin\theta(k)\cos\theta(k)\frac{d^3k}{8\pi^3} \tag{c. 10}$$

as combined with (c. 8) for $\theta(\vec{k})$ as a function of $g(\vec{k})$. The one electron energy for spin-up plane wave is

$$\varepsilon_{\vec{k}'}=\frac{\hbar^2|\vec{k}'|^2}{2m}-\int\frac{4\pi e^2}{|\vec{k}'-\vec{k}|^2}\cos^2\theta\frac{d^3k}{8\pi^3}. \tag{c. 11}$$

He has examined the solution of (c. 10) and proved that the paramagnetic state of an electron gas is always unstable to the formation of such a SDW having a wave vector

$$q=2k_F, \tag{c. 12}$$

i. e. twice the diameter of the Fermi sphere.

Since the theory of OVERHAUSER entirely ignores the presence of lattice, it is called a free elctron model in this thesis. However the OVERHAUSER's theory has a deep insight in the theory of ferro- or antiferromagnetism in transition metals and alloys. The nomenclature "free electron model", therefore, does not mean all the important aspects of his arguments.

C.2 Single-band model by TACHIKI and NAGAMIYA[29]

TACHIKI and NAGAMIYA, on the other hand, have considered a tight binding single-band model, for which they have taken into account the Umklapp process as being essentially important mechanism for stabilizing a helical spin arrangement. The helical exchange potential, whose periodicity is characterized by a wave vector $\vec{q}$, connects Bloch states in pairs :

$$\vec{k},\ \alpha\rightleftarrows\vec{k}+\vec{q}+\vec{G},\ \beta. \tag{c. 13}$$

where $\vec{G}$ is a reciprocal lattice vector which makes $\vec{k}+\vec{q}+\vec{G}$ come into the first Brillouin zone.

They have obtained the following self-consistency relation for the occurrence of helical spin arrangement :

$$\frac{g^2(\vec{k})}{U}=\frac{1}{N}\Sigma^{+}\frac{\pm g^2(\vec{k})}{\left[g^2(\vec{k})+x^2\right]^{\frac{1}{2}}}, \tag{c. 14}$$

where $g(\vec{k})$ is an exchange integral, U is the intra-atomic Coulomb integral in the same band, N is the number of atoms, x is defined in terms of unperturbed one-electron enegy $\varepsilon(\vec{k})$ as

$$x=\frac{1}{2}\left[\varepsilon(\vec{k}+\vec{q}+\vec{G})-\varepsilon(\vec{k})\right]. \tag{c. 15}$$

The double sign is taken + when k is inside the discontinuity surfaces and − when k is outside. The summation Σ^{+} takes over occupied states with $E^{+}(\vec{k})$ defined by

$$E^{+}(\vec{k})=\varepsilon(\vec{k})+x\mp(x^2+g^2)^{\frac{1}{2}}, \tag{c. 16}$$

where the double sign is taken in accordance with $x\gtrless 0$.

They calculated (c. 14) in the limit of $g\to 0$:

$$f(\vec{q})=\frac{1}{N}\Sigma^{+}\frac{1}{x}, \tag{c. 17}$$

as a function of $\vec{q}$, taking the number of electrons per atom n as a parameter. Assuming the Fermi surface to be spherical, n can be correlated with the Fermi momentum k_F. The values of q, which give maximum $f(q)$ for given n, determine the helical structure to be stabilized. They evaluated (c. 17) numerically for q's near 0 and near $2\pi/a$ for the Brillouin zone of a bcc crystal with various values of k_F.

C.3 Two-band model by LOMER[30]

On the basis of the calculation[57] of electron energy levels in bcc transition metals, LOMER[30] proposed the position of the Fermi surfaces in Cr. It mainly consists of an electron jacket around Γ and a hole octahedron around H. If a periodic modulation of SDW, whose wave vector is q, is introduced, there will be a mixing of Bloch waves between the pairs in different bands around Γ and H :

$$\vec{k},\ \alpha,\ \Gamma \rightleftarrows \vec{k}+\vec{q},\ \beta,\ H. \tag{c. 18}$$

This mixing modifies the wave functions and their one-electron energy according to the perturbation theory, resulting in the lowering of the total energy of the system. The lowering of energy will be largest for the wave vector $\vec{q}$, which shifts relative position of the two bands around Γ and H as shown in Fig. 20, in which the effective area of contact of the two Fermi surfaces is maximized.

The two-band model was later elaborated by FEDDERS and MARTIN[31], who formulated the criterion for the instability of paramagnetic state of an electron gas to the formation of SDW state with wave vector $\vec{q}$. The instability occurs at the $\vec{q}$ at which

$$R=-\frac{1}{\Omega}\sum_{k}v(0)\gamma^2\frac{f_a\left(k+\frac{1}{2}q\right)-f_b\left(k-\frac{1}{2}q\right)}{E_a\left(k+\frac{1}{2}q\right)-E_b\left(k-\frac{1}{2}q\right)} \tag{c. 19}$$

first becomes larger than one. In this expression, $1/\Omega$ is a normalization constant, $v(0)$ is Fourier transform of interaction potential equal to $4\pi e^2/\xi^2$ in which ξ is of the order of

FERMI-THOMAS momentum, γ is the average of overlap integral in the same band, i. e.

$$\int d^3r\, b_n\left(\vec{k}+\frac{1}{2}\vec{q},\ \vec{r}\right) b_n^*\left(\vec{k}'+\frac{1}{2}\vec{q},\ \vec{r}\right) e^{i([\vec{k}'-\vec{k}]_z)\vec{r}}$$

where $b_n(\vec{k},\ \vec{r})$ is a Bloch function labeled by the band indices (n), $[\vec{k}'-\vec{k}]_z$ is the reduced part belonging to the first Brillouin zone, $f(\vec{k})$ is the Fermi factor

$$f_n(\vec{k}) = [\exp \beta(E_n(\vec{k}) - \mu) + 1]^{-1}$$

and $E_n(\vec{k})$ is a HARTREE-FOCK energy associated with Bloch function $b_n(\vec{k},\ r)$.

Since only a small volume near the Fermi surface will contribute significantly to the sum (c. 19), the criterion can be expressed in terms of the Fermi velocities :

$$R \approx -\frac{e^2\gamma^2\pi}{2\xi^2 a^3 E_F (v_a + v_b)} S \ln(\pi/2\delta), \qquad \text{(c. 20)}$$

where v_a and v_b are the Fermi velocities of the two bands, δ is an average separation between the two surfaces as shown in **Fig. 20.** S is the area of close contact of the two surfaces (the area marked by S in **Fig. 20**) and a is half the cube edge in the lattice space, E_F is the Fermi energy.

FEDDERS and MARTIN have given the formula for T_N

$$k_B T_N = \frac{2\gamma_e \bar{v}\, \bar{k}_c f}{\pi} \exp(-1/\lambda) \qquad \text{(c. 21)}$$

where

$$\ln f = (K^2 + 2Kk_c - 6k_c^2)/4k_c^2$$

$$\bar{k}_c = [k_c(K - k_c)]^{\frac{1}{2}}$$

and

$$\lambda = \gamma^2 v(0) k_c^2 / 2\pi^2 v, \qquad \text{(c. 22)}$$

where k_c is some wave vector in the first Brillouin zone, a sort of average Fermi momentum, K is a radius of a sphere which approximates the first Brillouin zone, v and $\bar{v}$ are average velocities of v_a and v_b difined as

$$v = \frac{1}{2}(v_a + v_b)$$

$$\bar{v} = (v_a v_b)^{\frac{1}{2}}$$

and $\ln\gamma_e = 0.577$ which is Euler's constant.

They have shown that there is a linear relationship between the Néel temperature T_N and the magnetic moment μ at absolute zero temperature by the formula

$$g(T=0) = \pi v k_B T_N / \gamma_e \bar{v} \qquad \text{(c. 23)}$$

where g is energy gap of electron band, which is proportional to the magnetic moment μ.

References

1) C. G. SHULL and M. K. WILKINSON : *Rev. Mod. Phys.*, **25**, 100 (1953)
2) M. E. FINE, E. S. GREINER and W. C. ELLIS : *Trans. Amer. Inst. Min. Met. Eng.*, **191**, 56 (1951)
3) H. PURSEY : *J. Inst. Metals*, **86**, 362 (1960)
4) R. H. BEAUMON, H. CHIHARA and J. A. MORRISON : *Phil. Mag.*, **5**, 188 (1960)
5) L. M. CORLISS, J. M. HASTINGS and R. J. WEISS : *Phys. Rev. Letters*, **3**, 211 (1959)
6) V. N. BYKOV, V. S. GOLOVKIN, N. V. AGEEV, V. A. LEVDIK and S. I. VINOGRADOV : *Dokl. Akad. Nauk. SSSR*, **128**, 1153 (1959)——English transl., *Soviet Phys.——Doklady*, **4**, 1070 (1960)
7) G. E. BACON : *Acta Cryst.*, **14**, 823 (1961)
8) G. SHIRANE and W. J. TAKEI : *J. Phys. Soc. Japan*, **17**, Suppl., B-III, 35 (1962)
9) M. K. WILKINSON, E. O. WOLLAN, W. C. KOEHLER and J. W. CABLE : *Phys. Rev.*, **127**, 2080 (1962)
10) A. ARROTT, S. A. WERNER and H. KENDRICK : *Phys. Rev. Letters*, **14**, 1022 (1965)
11) T. J. BASTOW and R. STREET : *Phys. Rev.*, **141**, 510 (1966)
12) G. DE VRIES : *J. Phys. Radium*, **20**, 438 (1959)
13) M. A. TAYLOR : *J. Less-Common Metals*, **4**, 476 (1962)
14) L. E. DRAIN : *J. Phys. Radium*, **23**, 745 (1962)
15) J. S. KASPER and R. M. WATERSTRAT : *Acta Cryst.*, **9**, 289 (1956)
16) Y. HAMAGUCHI and N. KUNITOMI : *J. Phys. Soc. Japan*, **19**, 1849 (1964)
17) H. BJERRUM MØLLER, A. L. TREGO and A. R. MACKINTOSH : *Solid State Comm.*, **3**, 137 (1965)
18) R. G. BARNES and T. P. GRAHAM : *J. Appl. Phys.*, **36**, Part 2, 938 (1965)
19) F. HEINIGER, E. BUCHER and J. MULLER : *Phys. Letters*, **19**, 163 (1965)
20) T. SUZUKI : *J. Phys. Soc. Japan*, **21**, 442 (1966)
21) S. KOMURA and N. KUNITOMI : *J. Phys. Soc. Japan*, **20**, 103 (1964)
22) Y. HAMAGUCHI, E. O. WOLLAN and W. C. KOEHLER : *Phys. Rev.*, **138**, A 737 (1965)
23) S. KOMURA, N. KUNITOMI and Y. HAMAGUCHI : to be published in JAERI-memo.
24) S. KOMURA, Y. HAMAGUCHI and N. KUNITOMI : *Phys. Letters*, **24 A**, 299 (1967)
S. KOMURA, Y. HAMAGUCHI and N. KUNITOMI : to be published in *J. Phys. Soc. Japan*.
25) W. C. KOEHLER, R. M. MOON, A. L. TREGO and A. R. MACKINTOSH : *Phys. Rev.*, **151**, 405 (1966)
26) T. J. BASTOW : *Proc. Phys. Soc.*, **88**, 935 (1966)
27) A. W. OVERHAUSER : *Phys. Rev.*, **128**, 1437 (1962)
28) K. YOSIDA : *Progr. Theor. Phys.*, **28**, 759 (1962)
29) M. TACHIKI and T. NAGAMIYA : *Phys. Letters*, **3**, 214 (1963)
30) W. M. LOMER : *Proc. Phys. Soc.*, **80**, 489 (1962)
31) P. A. FEDDERS and P. C. MARTIN : *Phys. Rev.*, **143**, 245 (1966)
32) C. H. CHENG, C. T. WEI and P. A. BECK : *Phys. Rev.*, **120**, 426 (1960)
33) L. F. MATTHEISS : *Phys. Rev.*, **134**, A 970 (1964)
34) T. L. LOUCKS : *Phys. Rev.*, **139**, A 1181 (1965)
35) L. F. MATTHEISS : *Phys. Rev.*, **139**, A 1893 (1965)
36) The present experiments were mostly performed at Japan Atomic Energy Research

Institute by the present author and his colleagues. However some of the results, especially on neutron diffraction studies on Cr–Mn alloys, were performed by Dr. Y. HAMAGUCHI and his collaborators at Oak Ridge National Laboratory during his stay at the Laboratory.

37) N. KUNITOMI, Y. HAMAGUCHI, M. SAKAMOTO and S. KOMURA : *J. Phys. Soc. Japan*, **17**, Suppl., 8-II, 354 (1962)

38) G. E. BACON : *Neutron Diffraction*, second ed., Oxford at the Clarendon Press (1962)

39) J. M. HASTINGS, N. ELLIOTT and L. M. CORLISS : *Phys. Rev.*, **115**, 13 (1959)

40) R. M. MOON, W. C. KOEHLER and A. L. TREGO : *J. Appl. Phys.*, **37**, 1036 (1966)

41) The chemical analysis was performed by removing the chromium as chromylchloride from the specimens followed by the extraction-photometric method using oxyne or 2-methyl-oxyne at the suggestion by Dr. H. HASHITANI in the analytical chemistry laboratory in JAERI.

42) The rate of change in the number of electrons is slightly underestimated in the paper 21). Therefore the original values of change in the number of electrons in 21) should be multiplied by the factor 2 to get the present values.

43) R. MITSUDO, K. MOTIZUKI and T. NAGAMIYA : *J. Phys. Soc. Japan*, **20**, 710 (1965)

44) S. ASANO : to be published.

45) M. M. NEWMANN and K. W. H. STEVENS : *Proc. Phys. Soc.*, **74**, 290 (1959)
N. S. RAJAN, R. M. WATERSTRAT and P. A. BECK : *J. Appl. Phys.* **31**, 731 (1960)
S. ARAJS and G. R. DUNMYRE : *J. Appl. Phys.* **37**, 1017 (1966)
K. SCHRÖDER, M. J. YESSIK and N. P. BAUM : *J. Appl. Phys.*, **37**, 1019 (1966)

46) Y. ISHIKAWA, S. HOSHINO and Y. ENDOH : *J. Phys. Soc. Japan*, **22**, 1221 (1967)

47) W. HUME-ROTHERY and G. V. RAYNOR : *The structure of Metals and Alloys*, Institute of Metals, London (1956)

48) K. YOSIDA and A. WATABE, *Progr. Theor. Phys.*, **28**, 361 (1962)

49) H. MIWA : *Progr. Theor. Phys.*, **29**, 477 (1963)

50) R. J. ELLIOTT and F. A. WEDGEWOOD : *Proc. Phys. Soc.*, **81**, 846 (1963)

51) J. C. SLATER : *Phys. Rev.*, **82**, 538 (1951)

52) T. MATSUBARA and T. YOKOTA : *Proc. Intern. Conf. Theoret. Phys.*, Kyoto-Tokyo, Japan (1953)

53) E. FERMI : *Ric. Sci.*, **7**, 13 (1936)

54) O. HALPERN and M. H. JOHNSON : *Phys. Rev.*, **55**, 898 (1938)

55) W. C. KOEHLER : *Acta Cryst.*, **14**, 535 (1961)

56) S. HOSHINO and Y. YAMADA : *Nihon Buturi Gakkai-shi* [*Bulletin of Phys. Soc. of Japan*], **18**, 122 (1963)

57) J. H. WOOD : *Phys. Rev.*, **126**, 517 (1962)